

Electrically tunable MoSe₂/WSe₂ heterostructure-based quantum dot

Katarzyna Sadecka,^{1,2,*} Maciej Bieniek,¹ Paulo E. Faria Junior,³
Arkadiusz Wójs,¹ Paweł Hawrylak,² and Jarosław Pawłowski^{1,†}

¹*Institute of Theoretical Physics, Wrocław University of Science and Technology,
Wybrzeże Wyspiańskiego 27, 50-370 Wrocław, Poland*

²*Department of Physics, University of Ottawa, Ottawa, K1N6N5, Canada*

³*Institute of Theoretical Physics, University of Regensburg, 93040 Regensburg, Germany*

(Dated: December 23, 2024)

We describe here a theory of a quantum dot in an electrically tunable MoSe₂/WSe₂ heterostructure. Van der Waals heterostructures allow for tuning their electronic properties beyond their monolayer counterparts. We start by determining their electronic structure using density functional theory. We obtain the type-II band alignment and close in energy conduction band minima (valleys) at the *K* and *Q* points in the Brillouin zone. The valence band maxima, also energetically close, are located at the *K* and Γ points. By analyzing the Kohn-Sham wavefunctions, we describe the layer, spin, and orbital contributions. Next, we construct an *ab initio*-based tight-binding model, which helps us to better understand the complexity of the interlayer interactions. We determine the effect of a vertical electric field, showing that vertical gating enables control of valleys extrema and their occupancy. Finally, we employ the tight-binding model to investigate laterally gated quantum dots and analyze the influence of a perpendicular electric field on their energy spectrum. Our results demonstrate that tuning the electric field enables control over the valley character of the quantum dot states, selectively localizing them in either the *K* or *Q* valleys, as evidenced by their characteristic degeneracies and wavefunctions.

Keywords: 2D materials, transition metal dichalcogenides, heterostructures, quantum dots, tight-binding model

I. INTRODUCTION

Single layers of transition metal dichalcogenides (TMDCs) are two-dimensional (2D) semiconductors enabling the exploration of many physical phenomena [1–5]. For example, low-energy massive Dirac fermions possess a spin-valley pseudospin structure [6–15] that can be controlled using electromagnetic fields and accessed using polarized light. TMDCs are also the basic “blocks” for the construction of van der Waals (vdW) heterostructures [16, 17], in which many aspects of a monolayer controlability are preserved, in contrast to homobilayers. These heterostructures can be superior in some applications due to better control of electronic properties via electric field, light emission from interlayer excitons closer to telecommunication band, and enhanced valley coherence time [18–21]. Longer exciton lifetime opens new avenues for engineering long-range exciton transport and strongly interacting artificial bosonic simulators [22].

Quantum information platforms require initialization and control over individual quantum states. Electrical confinement and manipulation of charge carriers are essential factors. Circularly polarized light can populate (initialize) a given valley [23, 24], nevertheless optical coupling of valley degrees of freedom in TMDCs can be realized only indirectly. However, valley coupling can be achieved electrically in TMDC-based quantum dots

(QDs) [5, 25–35]. Different methods of realizing the electrical control over the valley degree of freedom have been proposed, such as applying a sharp confining potential [10, 31], creating a lateral heterostructure [36], or by the coupling with defect states [37, 38]. It has been shown that spin–valley locked quantized conductance [28, 39, 40] and electrical control over charged excitons [29] can be achieved experimentally. Furthermore, theoretical studies of electrically defined TMDC-based QDs have shown potential to realize qubits, including spin qubits, valley qubits and hybrid spin–valley qubits [10, 11, 32, 41, 42]. We note that the previous works focused on the *K*-valley states [10, 11, 31, 32, 40, 43–45]. In this work, we discuss the possibility of controlling different valley minima using external electric field.

One of the promising heterostructures is composed of MoSe₂ and WSe₂ monolayers [20, 22, 46–80]. Having similar lattice constants (3.288 Å and 3.286 Å) [81], when stacked using the exfoliation technique, they can create long-range order moiré potential [48, 59, 73, 82–84], however relaxation/annealing-induced atomic reconstruction can make regions that are commensurate [85, 86]. In contrast, CVD grown samples show no moiré pattern [87]. Analyzed experimentally in recent years, MoSe₂/WSe₂ heterostructures enable the development of novel optoelectronic [18–21, 46, 54, 55, 88–103], valleytronic [47, 104, 105], and quantum computing [106–112] devices.

On the theoretical side, several important advancements have already been achieved. An accurate approach using density functional theory (DFT) established the band gap of type II: the conduction band (CB) minimum from MoSe₂ layer, the valence band (VB) maximum from

* katarzyna.sadecka@pwr.edu.pl

† jaroslaw.pawlowski@pwr.edu.pl

WSe₂ layer. It is also known that the values of spin-orbit gaps are inherited from monolayers. As usual for 2D materials, in which the electron-electron interactions are strong, it is less clear whether the (optical) gap extrema are in K -points or some other valleys contribute to the physics around the Fermi level, usually Γ valley at the VB and so called $Q/\Sigma/\Lambda$ points between K and Γ in the CB. Several works [70, 113–119] studied the problem of the optical properties of this system. While the state-of-the-art *ab initio* methods are invaluable, it is much more convenient to use the low-energy methods. For TMDCs bilayers several works established how to approach the construction of the tight-binding (TB) and $k \cdot p$ models [120–123]. Focusing on the TB models that offer a good trade-off between accuracy and performance, there are several works discussing the TB models for homobilayers, e.g. bilayer MoS₂ [124–130]. Surprisingly, we are not aware of any model discussing interactions between two different TMDC monolayers on the atomistic level in a full orbital basis, taking into account both d and p orbitals. This problem is non-trivial due to the two seemingly contradictory observations: one being that since the interlayer interactions are weak (vdW) it should be possible to understand the interlayer coupling using the nearest neighbour (NN) p_z orbitals on chalcogenide atoms; second stating that majority of physics of these materials can be understood in terms of the d orbitals localized on metal atoms. In order to get better understanding, we constructed a full interlayer-interaction model that is consistent with the monolayer basis, consisting of both metal and chalcogen orbitals.

The paper is organized as follows. In Section II we describe the electronic properties of MoSe₂/WSe₂ heterostructure using DFT. We follow by construction of the TB model in Section III. In Section IV we discuss the effect of a perpendicular electric field. Using the TB model, in Section V we describe a lateral gated quantum dot. We demonstrate that the applied vertical electric field enables control over the QD energy spectrum by tuning the valley character of the low-energy states, transitioning between K (2-fold degenerate) and Q (6-fold degenerate) configurations. Finally, in Section VI we summarize our main findings.

II. AB INITIO BAND STRUCTURE OF MOSE₂/WSE₂ HETEROSTRUCTURE

In this section, we describe the electronic properties of MoSe₂/WSe₂ from DFT. For computational details see Appendix A. The three-dimensional (3D) view of the system is shown in Fig. 1(a). We study the energetically preferable AB stacking [131], in which the metal atoms of one layer are located under the chalcogen atoms of the other layer. As presented in Fig. 1(b), the unit cell (UC) consists of 6 atoms belonging to the distinct layers. The top view of the system is shown in Fig. 1(c), representing the honeycomb lattice. The primitive vectors of the real

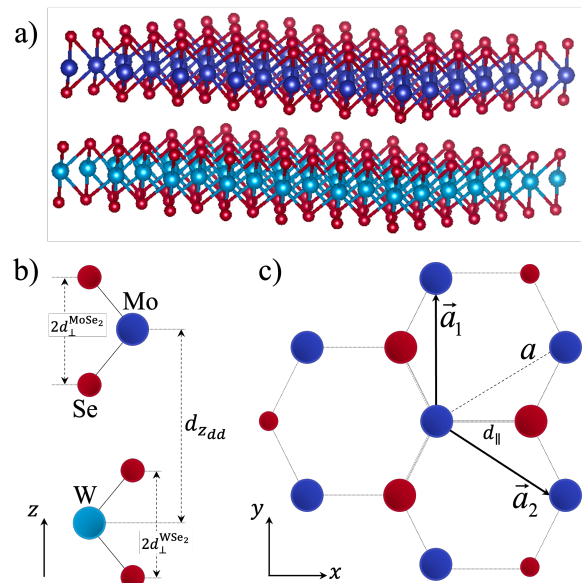


FIG. 1. Geometry of the MoSe₂/WSe₂ heterostructure: (a) three-dimensional (3D), (b) side, and (c) top views. Top and bottom layers are MoSe₂ and WSe₂, respectively. Molybdenum (tungsten) metal atoms are represented by dark (light) blue dots, while selenium atoms are shown in red. The interlayer distance has been defined as d_{zdd} . The unit cell is shown in (b). Primitive lattice vectors \vec{a}_1 , \vec{a}_2 are chosen as denoted in (c).

space lattice are $\vec{a}_1 = (0, a)$ and $\vec{a}_2 = (a\sqrt{3}/2, -a/2)$, with $a = d_{||}\sqrt{3}$ being the lattice constant. The K point is then given by $\vec{K} = (0, 4\pi/3a)$. We note that the lattice mismatch in the MoSe₂/WSe₂ heterostructure is negligibly small, $\Delta a < 0.001 \text{ \AA}$, thus causing no significant strain. The lattice constant has been set to $a = 3.323 \text{ \AA}$. In order to determine the interlayer distance, we studied the total energy as a function of layers distance [132], obtaining energy minimum for $d_{zdd} = 6.400 \text{ \AA}$. Metal-chalcogen distances d_{\perp} are 2.869 \AA and 2.880 \AA for top and bottom layers, respectively.

A. Layer-spin-orbital properties

Here we analyze the bandstructure of MoSe₂/WSe₂ heterostructure, as presented in Fig. 2. We find that it is characterized by the CB minima at K and Q points that are close in energy, separated by 1.8 meV. The VB maxima at K and Γ points are separated by 35.5 meV. Fig. 2(a) shows the spin-resolved electronic structure. The direct K - K energy gap is determined to be $E_g = 1.04 \text{ eV}$, which is smaller compared with separate monolayers, for which we obtained $E_g^{\text{MoSe}_2} = 1.34 \text{ eV}$ and $E_g^{\text{WSe}_2} = 1.24 \text{ eV}$. It is worth mentioning that in K points bands around the fundamental gap belong to different layers, as will be discussed later. The intralayer K -valley spin splittings due to the atomic spin-orbit cou-

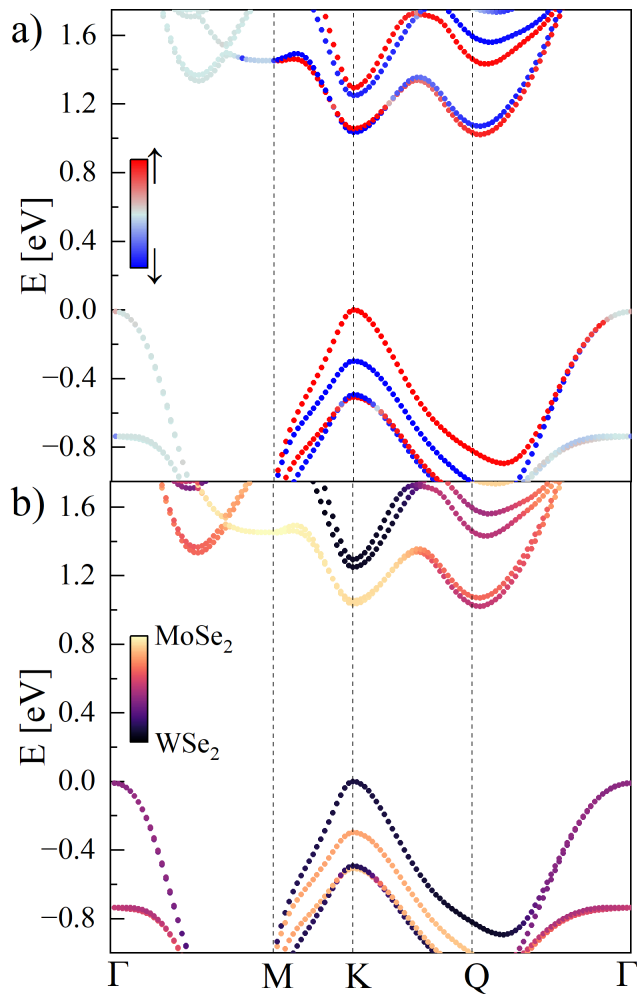


FIG. 2. *Ab initio* electronic structure of the MoSe₂/WSe₂. The energy spectrum is presented on the path Γ -M-K-Q- Γ . The two panels show (a) spin- and (b) layer-resolved electronic structures. Both spin and layer are decoded by color, where red/blue denotes spin up/down, while yellow/black denotes MoSe₂/WSe₂ layer, respectively.

pling (SOC) in both CB and VB are $\Delta_{\text{SOC}}^{\text{CB}} = 12$ meV and $\Delta_{\text{SOC}}^{\text{VB}} = 211$ meV for MoSe₂-localized bands, while for WSe₂ $\Delta_{\text{SOC}}^{\text{CB}} = 30$ meV and $\Delta_{\text{SOC}}^{\text{VB}} = 473$ meV. The values of spin-orbit splitting are similar to those of single layers. We note that for the direct transition across the fundamental gap K - K spin is flipped, while for the transition from K to Q the spin is parallel.

Furthermore, Fig. 2(b) presents the details of the layer contributions. We note the type-II band alignment, where around K valley electrons in the bottom of the CB belong to the MoSe₂ layer, while holes in the top of the VB belong to the WSe₂ layer, in agreement with previous works [9, 117, 133, 134]. While around the K valley we observe a strong spin-layer localization for both electrons in CB and holes in VB, in the Q valley electrons are delocalized between distinct layers, as shown in Fig. 2(b).

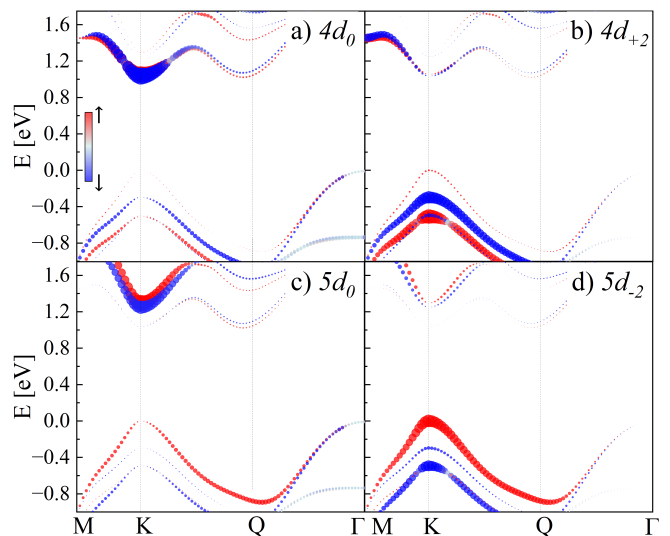


FIG. 3. Orbital contribution for the leading orbitals from both layers: (a) $4d_{m=0}$ and (b) $4d_{m=+2}$ from molybdenum, and (c) $5d_{m=0}$ and (d) $5d_{m=-2}$ from tungsten. Color denotes spin.

Moreover, detailed analysis of the density ρ_k^n (defined in the Appendix A) shows that the spin of the electron in Q is mixed ($\approx 20\%$ admixture), contrary to K valley.

Using the Kohn-Sham wavefunctions projected onto localized orbitals, the orbital-resolved decomposition of wavefunctions has been performed, see Appendix A and Fig. 3. Similar to the case of a single layer of TMDCs [7, 9], the main contribution to the bands around the Fermi level comes from the symmetric (even) orbitals. The CB is mainly composed of the metal orbitals, $4d_{m=0}$ for Mo and $5d_{m=0}$ for W, depicted in Fig. 3(a,c), while the contribution to the VB comes mainly from the $4d_{m=\pm 2}$ orbitals for Mo and $5d_{m=\pm 2}$ for W, shown in Fig. 3(b,d). Due to the AB stacking the dominant orbital contribution around valley K in the valence band is $4d_{m=+2}$ for MoSe₂ layer and $5d_{m=-2}$ for WSe₂ layer, in line with simple picture of opposite valleys on top of each other (however, this does not mean simple valley-layer locking due to the strong layer localization effect). The orbital contribution around the Q valley is more complex, reflecting the effect of electron delocalization between distinct layers. Detailed values of the orbital contributions to energy bands at high symmetry points are given in Tab. I in Appendix A.

III. TIGHT-BINDING MODEL

In the following section we construct the *ab initio*-based TB model for a type-II TMDC heterostructure. This approach allows us to understand the interlayer interactions and the effect of an applied electric field. It also opens the possibility to study heterobilayer-based nanostructures.

A. Orbital basis

Building on previous works on monolayer TMDCs [7–9, 31], we construct a two-layer, spinfull, even-odd orbital model of the AB stacked heterostructure in next-nearest neighbour (NNN) hopping approximation, for both inter- and intralayer hoppings. The electron wavefunction is defined as a linear combination of localized atomic orbitals ψ_l (for details see Appendix B) and has the following form [7]:

$$\begin{aligned} \varphi_k^p(\vec{r}) &= \frac{1}{\sqrt{N_U}} \sum_{i=1}^{N_U} \sum_{l=1}^{N_l} e^{i\vec{k}\cdot\vec{U}_{i,l}} A_{k,l}^p \psi_l(\vec{r} - \vec{U}_{i,l}) = \\ &= \sum_{l=1}^{N_l} A_{k,l}^p \phi_{k,l}(\vec{r}), \end{aligned} \quad (1)$$

where p denotes bands, \vec{k} is a wavevector on the 2D Brillouin zone (BZ), and $\phi_{k,l}(\vec{r})$ are the orbital Bloch functions. The number of UCs is N_U , while N_l corresponds to the number of orbitals on different sublattices. The orbitals are localized at $\vec{U}_{i,l} = \vec{U}_i + \vec{\tau}_l$, where U_i are the UC coordinates, and τ_l denotes the l -th atomic orbital positions inside of each UC. The coefficients $A_{k,l}^p$ are solution to the TB Hamiltonian, Eq. (3), $H_{\text{hetero}}(\vec{k})\vec{A}_k^p = \varepsilon_k^p \vec{A}_k^p$. Based on the DFT studies we have taken the d metal atom orbitals with $m = \{0, \pm 1, \pm 2\}$ and the p chalcogen dimers constructed out of orbitals with $m = \{0, \pm 1\}$. Thus, the number of orbitals on metal atom is 5 and on chalcogen dimer sites is 6 (including even and odd combinations).

It is convenient to separate the sum over orbitals \sum_l between two subspaces, even $\mathcal{H}_{\text{even}}$ and odd \mathcal{H}_{odd} with respect to the single layer metal planes. The constructed basis is ordered in the following way: $\{m_d = -2, 0, 2, m_p = -1, 0, 1\}$ for even subspace, and $\{m_d = -1, 1, m_p = -1, 0, 1\}$ for the odd subspace. The chalcogen dimers X_2 for p orbitals are defined for both subspaces as $m_{p+1} = (|m_{p+1}^{X(1)}\rangle \pm |m_{p+1}^{X(2)}\rangle)/\sqrt{2}$, $m_{p_0} = (|m_{p_0}^{X(1)}\rangle \mp |m_{p_0}^{X(2)}\rangle)/\sqrt{2}$, and $m_{p-1} = (|m_{p-1}^{X(1)}\rangle \pm |m_{p-1}^{X(2)}\rangle)/\sqrt{2}$, where the $+/-$ sign corresponds to the even/odd subspace and 1/2 index to the top/bottom atom within the X_2 dimer. The full spinless even-odd wavefunction of the monolayer can be thus written as $\varphi_k^p(\vec{r}) = [\varphi_k^{p,\text{ev}}(\vec{r}), \varphi_k^{p,\text{odd}}(\vec{r})]^T$. We note that in this chiral basis we need to use linear combinations of standard Slater-Koster [135] hopping integrals.

B. Spinfull monolayer Hamiltonian

Monolayer Hamiltonians for both MoSe₂ and WSe₂ with SOC can be written, following previous works, as

[7, 9, 31]:

$$H_{\text{MX}_2} = \begin{bmatrix} H_{\uparrow}^{\text{ev}} & 0 & 0 & H_{\downarrow}^{\text{ev-odd}} \\ & H_{\uparrow}^{\text{odd}} & H_{\uparrow\downarrow}^{\text{odd-ev}} & 0 \\ & & H_{\downarrow}^{\text{ev}} & 0 \\ & & & H_{\downarrow}^{\text{odd}} \end{bmatrix}. \quad (2)$$

The Hilbert space of \hat{H} defined in Eq. (2) is given by $\mathcal{H}_{\text{MX}_2} = (\mathcal{H}_{\text{even}} \oplus \mathcal{H}_{\text{odd}}) \otimes \mathcal{H}_{\text{spin}}$, thus it is characterized by the dimension $(6 + 5) \times 2$, and hence it is represented by a 22×22 matrix. The atomic SOC has been also included. It is defined as $\hat{H}_{\text{SOC}} = \sum_a \lambda_a / \hbar \hat{\mathbf{L}}_a \cdot \hat{\mathbf{S}}_a$ [31], with λ_a depending on the specific atom, $\hat{\mathbf{L}}_a$ being the atomic orbital angular momentum operator, and $\hat{\mathbf{S}}_a$ the spin operator. Further details on constructing the monolayer Hamiltonian can be found in the Appendix B.

C. Heterostructure Hamiltonian

The TB Hamiltonian for MoSe₂/WSe₂ can be written in a block form, emphasizing distinct layers and the interlayer interaction, as:

$$\hat{H}_{\text{hetero}} = \begin{bmatrix} \hat{R}_z^\pi H_{\text{MoSe}_2} & H_{\text{inter}} \otimes \mathbf{1}_\sigma \\ & H_{\text{WSe}_2} \end{bmatrix}, \quad (3)$$

To incorporate AB stacking we choose to rotate the MoSe₂ monolayer by π , thus rotating the MoSe₂ Hamiltonian block: $\hat{R}_z^\pi H_{\text{MoSe}_2}$, in contrast to the normal H_{WSe_2} orientation. Full form of both Hamiltonians is derived in Appendix B, where for clarity we use $\hat{R}_z^\pi H_{\text{MoSe}_2} = H^{(\pi)}$. The coupling between the distinct layers is denoted by H_{inter} which is the same for both spin blocks. All in all, the Hilbert space is a sum of $\mathcal{H}_{\text{MoSe}_2} \oplus \mathcal{H}_{\text{WSe}_2}$, thus, it is characterized by the total dimension $22 + 22$.

D. Interlayer coupling

We now move to construct a TB theory of the interlayer interactions. We include up to NNNs interaction, which, e.g., includes interlayer metal-metal interaction. The coupling between MoSe₂ and WSe₂ layers is defined in a block form as:

$$H_{\text{inter}} = \begin{bmatrix} H_{dd}^{\text{ev-ev}} & H_{dp}^{\text{ev-ev}} & H_{dd}^{\text{ev-odd}} & H_{dp}^{\text{ev-odd}} \\ H_{pd}^{\text{ev-ev}} & H_{pp}^{\text{ev-ev}} & H_{pd}^{\text{ev-odd}} & H_{pp}^{\text{ev-odd}} \\ H_{dd}^{\text{odd-ev}} & H_{dp}^{\text{odd-ev}} & H_{dd}^{\text{odd-odd}} & H_{dp}^{\text{odd-odd}} \\ H_{pd}^{\text{odd-ev}} & H_{pp}^{\text{odd-ev}} & H_{pd}^{\text{odd-odd}} & H_{pp}^{\text{odd-odd}} \end{bmatrix}, \quad (4)$$

with the interlayer couplings between Mo and W metal atoms (dd), chalcogen dimers (pp) and metal-chalcogen dimer interactions (pd/dp). The details of the Hamiltonian (4) can be found in Appendix C.

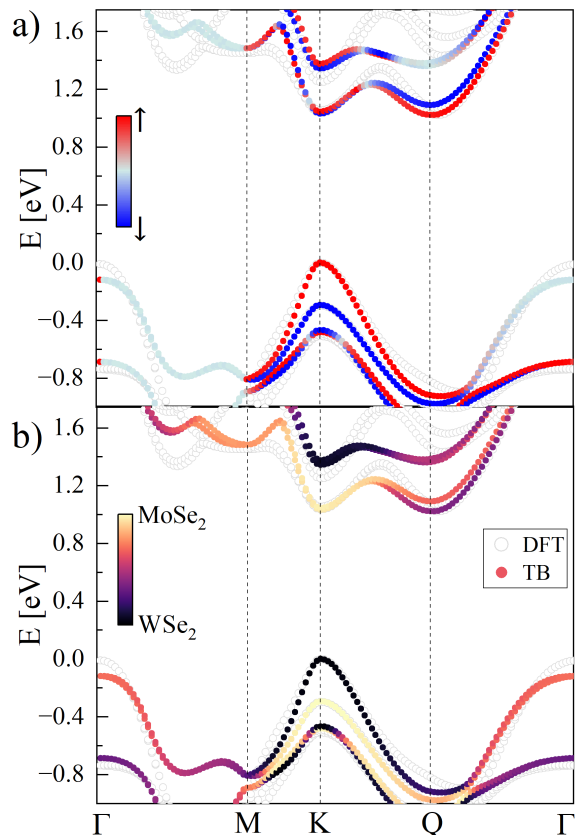


FIG. 4. Electronic structure of the MoSe₂/WSe₂ in the TB model. Panels present (a) spin and (b) layer resolved band structures. Both spin and layer are represented by color, where red/blue denotes spin up/down, while yellow/black denotes MoSe₂/WSe₂ layer, respectively. DFT results are given by open circles for reference. The parameter set used here is given in Appendix C in Tab. II.

E. Tight-binding model dispersion and spin-layer-orbital properties

Next we parametrize 26 intralayer and 9 interlayer Slater-Koster parameters, as well as 4 SOC strengths, as listed in Tab. II. This parameter set has been determined by fitting the TB model to the DFT results, described in Section II, using the differential evolution (DE) method [136]. We choose the parameters focusing on obtaining the degenerate CB minima around K and Q valleys and VB maxima around K and Γ . Moreover, we ensure the correct spin ordering of bands by including an additional term in the DE loss function:

$$\mathcal{L}_{\text{DE}} = \sum_{p \in \mathcal{P}} \sum_{\vec{k} \in \mathcal{K}} \left(\lambda_1 \left| \varepsilon_{\vec{k}}^p - \varepsilon_{\vec{k}}^{p, \text{DFT}} \right| + \lambda_2 \left| \langle \varphi_{\vec{k}}^p | \hat{\sigma}_z | \varphi_{\vec{k}}^p \rangle - \sigma_z^{\text{DFT}} \right| \right), \quad (5)$$

where the summation goes over selected subbands \mathcal{P} close to the bandgap, and subset \mathcal{K} of \vec{k} -points located nearby

the high symmetry points (K/K' , Q , and Γ) within the BZ. The $\lambda_1 = 1.0$ (eV⁻¹) term focuses on TB energies $\varepsilon_{\vec{k}}^p$ (bands) fitting to the DFT results, while the $\lambda_2 = 0.2$ regularizer tries to enforce the appropriate spin ordering in the TB eigenstates $\varphi_{\vec{k}}^p$, corresponding to these energies.

We obtain the single-particle spectrum and wavefunctions in the TB approximation by diagonalizing the Hamiltonian given by Eq. (3). Fig. 4 presents the spin-resolved TB electronic structure. The microscopic details of spin and layer contributions stay in agreement with the *ab initio* results. While the CB is characterized by a degenerate minima for K and Q valleys, in the VB maxima for K and Γ are split more than in DFT. The direct K - K energy gap is of the order of 1.03 eV. The spin-layer ordering of bands around the energy gap in K point has been captured correctly. Furthermore, while the direct K - K transition from the top VB to the bottom CB is dark due to spin, the indirect transition K - Q is bright due to spin, as shown in Fig. 4(a). The splittings of bands due to the SOC are consistent with those from DFT. Fig. 4(b) presents the microscopic details of the layer contribution. We confirm the type-II band alignment in our TB model. We note that the effect of the electron delocalization between layers in CB for the Q point has been captured correctly.

In the next step, we perform the orbital-resolved decomposition of wavefunctions, checking the leading orbital for each k point and each band. In agreement with the DFT results (see Section II), the main orbital contribution to the low-energy bands for the high symmetry points K and Q comes from the symmetric (even) orbitals. While the contribution to the VB comes mainly from the metal atom orbitals $4d_{m=0}$ for Mo and $5d_{m=0}$ for W, the CB is mainly composed of $4d_{m=\pm 2}$ orbitals for Mo and $5d_{m=\pm 2}$ for W. Further details of orbital contributions to the energy bands at the K and Q points are presented in Appendix C in Tab. III.

We realize that our full 44×44 TB model is complicated and might be challenging for implementation. While we leave a systematic reduction of it to a future work, we offer a simplified interlayer coupling analysis, that couples even blocks of orbitals in monolayers. This allows to study even-only TB model, which has 6 orbitals per layer per spin. We also simplified the interlayer interaction to capture most important orbital couplings. Details and behavior of such simplified TB model are studied in Appendix E.

IV. ELECTRIC FIELD EFFECT

In the following section we show that the energetic ordering of valleys can be controlled by applied vertical electric field. We introduce this field to the TB model by adding H_E term. The field E_z creates negative and positive voltages $V_E(z) = E_z z$ at the lower and upper TMDC layers, e.g., generated by vertical gates placed above and below (substrate) the heterostructure. We

set $V_E(z = d_{z_{ad}}/2) = 0$, such that on the metal atoms belonging to the upper layer the voltage is given as $+\frac{1}{2}E_z d_{z_{ad}}/\varepsilon$, while for the metal atoms of the bottom layer the voltage is $-\frac{1}{2}E_z d_{z_{ad}}/\varepsilon$. We assume typical dielectric screening for TMDCs materials as $\varepsilon \simeq 7$ [137].

A. Tight-binding model in electric field

Following Ref. [31], we write the electric field block H_E for both layers as (same for both spin components):

$$\hat{H}_E = \frac{1}{\varepsilon} \begin{bmatrix} H_E^{\text{MoSe}_2} \otimes \mathbf{1}_\sigma & 0 \\ 0 & H_E^{\text{WSe}_2} \otimes \mathbf{1}_\sigma \end{bmatrix}, \quad (6)$$

with

$$H_E^{\text{MoSe}_2} = \begin{bmatrix} \hat{V}_E^{\text{ev}} & \hat{V}_E^{\text{ev-odd}} \\ & \hat{V}_E^{\text{odd}} \end{bmatrix}, \quad H_E^{\text{WSe}_2} = \begin{bmatrix} -\hat{V}_E^{\text{ev}} & \hat{V}_E^{\text{ev-odd}} \\ & -\hat{V}_E^{\text{odd}} \end{bmatrix}.$$

Here \hat{V}_E^{ev} and \hat{V}_E^{odd} are just diagonal blocks with the same element on the diagonal $E_z \frac{1}{2} d_{z_{ad}}$, i.e., $\hat{V}_E^{\text{ev}} = E_z \frac{1}{2} d_{z_{ad}} \text{diag}(1, 1, 1, 1, 1, 1)$, while for $\hat{V}_E^{\text{odd}} = E_z \frac{1}{2} d_{z_{ad}} \text{diag}(1, 1, 1, 1, 1)$. The block $\hat{V}_E^{\text{ev-odd}}$ couples even and odd orbital subspace, with $V_{X_2} = \frac{1}{2}(V_{X^{(1)}} - V_{X^{(2)}})$ being the potential difference between chalcogen atoms in the dimer:

$$\hat{V}_E^{\text{ev-odd}} = \begin{bmatrix} 0 & 0 & 0 & 0 & 0 \\ 0 & 0 & 0 & 0 & 0 \\ 0 & 0 & 0 & 0 & 0 \\ 0 & 0 & V_{X_2} & 0 & 0 \\ 0 & 0 & 0 & V_{X_2} & 0 \\ 0 & 0 & 0 & 0 & V_{X_2} \end{bmatrix}. \quad (7)$$

The transformation from the single atom basis to our, i.e., the one using dimers, is described in Appendix D.

B. Effect of electric field on heterostructure: DFT and TB comparison

Valley K , Q , and Γ states evolution as a function of electric field E_z is presented in Fig. 5. We obtain satisfying agreement between the DFT results – Fig. 5(a), and the TB model – Fig. 5(b,c). To set the stage, we set the top of the VB in K point to 0 as a reference independently for each value of the electric field. For both DFT and TB we observe a clear trends in both VB and CB. For large negative values of E_z we observe VB maximum at K and CB minimum also at K . When electric field is increased, CB minimum switches between K and Q valleys. Similar effect is observed in VB, where VB maximum switches between K and Γ valleys. This establishes MoSe₂/WSe₂ heterostructure as an interesting multi-valley system in which occupation of different type of valleys can be controlled using moderate electric field.

Focusing now on spin properties, we note that the applied electric field does not change the spin orientation

for K valley for both VB and CB, as shown in Fig. 5(b). Contrary to that, for negative applied E_z the spin-mixing effect at the Q point is observed. The values of SOC splittings in K point of the CBs remain almost constant, while in the VBs they are strongly affected by the applied field. In the Q point the spin-splitting between the two CBs increases with positive E_z . Moreover, we notice the flip of spin across the gap, i.e. the lowest CB in the K point giving spin-dark, momentum-bright optical transition become spin-bright, momentum dark as the E_z increases.

In the next step we analyze evolution of the layer contribution, accessible in TB – see Fig. 5(c). First we note that electric field couples and mixes CB much stronger than VB. Focusing on CB, the K point comes mainly from MoSe₂, but for large E_z it can be strongly admixed by WSe₂ layer. For the Q valley, the layer contribution is mixed already at $E_z = 0$ and can be tuned continuously with the field applied. We note that the occupation of the CB K and Q valleys implies not only valley switching, but also switching between layer-localized to layer-delocalized type of bands.

Now we move to the analysis of CBs in E_z across the whole BZ, summarized in Fig. 5(d-i). We start with the system with no electric field applied, as presented in Fig. 5(d,e). In accordance with spin-valley locking, the two non-equivalent valleys K and K' differ by spin, as presented Fig. 5(e). In the CB each of them is surrounded by three Q points, creating a system of 6 non-equivalent Q points in the BZ. Also, K and Q valleys are almost degenerate in energy, as can be observed in Fig. 5(d). Next we apply a moderate electric field $E_z = -2.8$ V/nm – see Fig. 5(f,g). We observe breaking of the degeneracy between the energy minima for K and Q valleys. Furthermore, in Fig. 5(g) we observe the change of spin for the Q valleys, which stays in agreement with the flip of the two bottom CBs around Q observed in Fig. 5(b). Finally, for electric field $E_z = 2.8$ V/nm – Fig. 5(h,i), we observe the effect of breaking the energetic degeneracy in favor of Q valleys. This allows for E_z -field controlled occupation of the Q -valleys.

It should be also noted that a similar CB landscape composed of three valleys close to each K -point emerges in a bilayer graphene subjected to a perpendicular electric field, as a result of interplay between trigonal warping and E_z -field induced band gap [138]. These triple degenerate states have been studied theoretically [139, 140] and experimentally [141–143].

As previously noted, the energy evolution of the K point as a function of the electric field for states below (above) valence (conduction) band exhibits discrepancies between the full TB model and DFT, as shown in the bottom panels of Fig. 6(a,b). For the VB-1 (one band below the VB maximum) and VB-2 states at $E_z \approx -1.5$ V/nm DFT predicts a strong anticrossing for same-spin states (blue), an effect not captured by the full TB model. We attribute this discrepancy to differences in the layer and orbital contributions arising from the

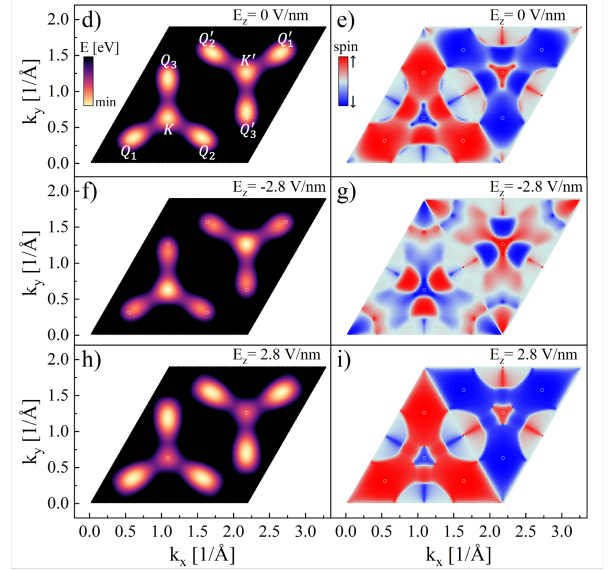
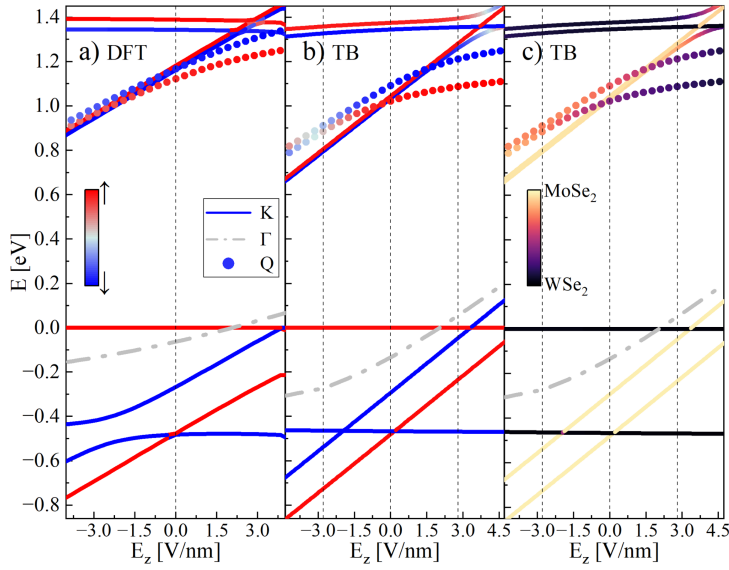


FIG. 5. The effect of a vertical electric field on the electronic structure. (a-c) Energies of selected bands are presented as a function of the applied E_z , following Ref. [134], for K , Q and Γ . Schemes presented for both (a) DFT results and (b,c) TB ones. Different type of lines represent K , Q and Γ valleys. Colors correspond to (a,b) spin, and (c) layer compositions, respectively. Due to the degeneracy of VB in the Γ point, the spin-/layer-resolved notation was not introduced. The vertical dashed lines denote to the electric field 0 and ± 2.8 V/nm. (d,f,h) Energy and (e,g,i) spin color maps (textures) of the lowest CB presented on the whole BZ for 3 different values of applied electric field: (d,e) $E_z = 0$ V/nm, (f,g) $E_z = -2.8$ V/nm, and (h,i) $E_z = 2.8$ V/nm, respectively. White circles correspond to the selected high symmetry points, denoted on the plots.

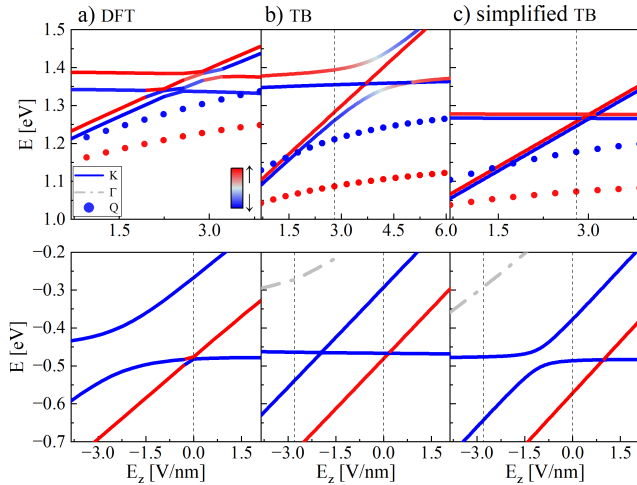


FIG. 6. Analysis of anti-crossing of K -point states in electric field. Top panel shows zoom into conduction band and lower one for valence band. Column (a) shows band evolution obtained using DFT, (b) - full TB model and (c) - simplified TB model. Note that color denotes spin and electric field on x -axis is different between top and bottom panels.

Slater-Koster parametrization used. However, in the simplified TB model (introduced in Appendix E), where the parametrization is different (see Tab. II), the anticrossing of bands is reproduced, as illustrated in Fig. 6(c).

V. ELECTRICALLY TUNABLE LATERALLY GATED QUANTUM DOT

We have demonstrated how electric field perpendicular to the MoSe₂/WSe₂ layers shifts the relative energies of different valleys. In this section, we leverage this effect in a lateral gate-defined QD. We investigate this system using the approach outlined in Refs. [31, 33–35, 40, 44, 144]. We begin with the MoSe₂/WSe₂ computational rhombus, which serves as the basis for defining Bloch functions in k -space. These functions are subsequently employed to describe the states of the gated QD and to analyze the effect of the applied vertical electric field, presented in Fig. 7.

To describe the QD we start by creating the rhomboidal real-space computational box consisting of MoSe₂ and WSe₂ atoms, depicted in Fig. 7(a). We impose the periodic boundary conditions connecting the opposite edges of the rhombus, thus giving us a set of allowed k -vectors. We expand the electron wavefunction in the basis of Bloch functions $\varphi_{\vec{k}}^p(\vec{r})$, see Eq. (1), built of WSe₂ and MoSe₂ atomic orbitals. For each \vec{k} wavevector we diagonalize the Hamiltonian given in Eq. (3) and obtain bulk electronic bands $\varepsilon_{\vec{k}}^p$ and eigenvectors $A_{\vec{k},l}^p$. We confine electrons in a gate-defined lateral Gaussian potential $V_{QD} = U_{QD}(1 - \exp(-r^2/\sigma_{QD}^2/2))$, presented in Fig. 7(b). The basis of the band states of the bulk system are functions $\varphi_{\vec{k}}^p(\vec{r}) = \sum_l A_{\vec{k},l}^p \phi_{\vec{k},l}(\vec{r})$, where l de-

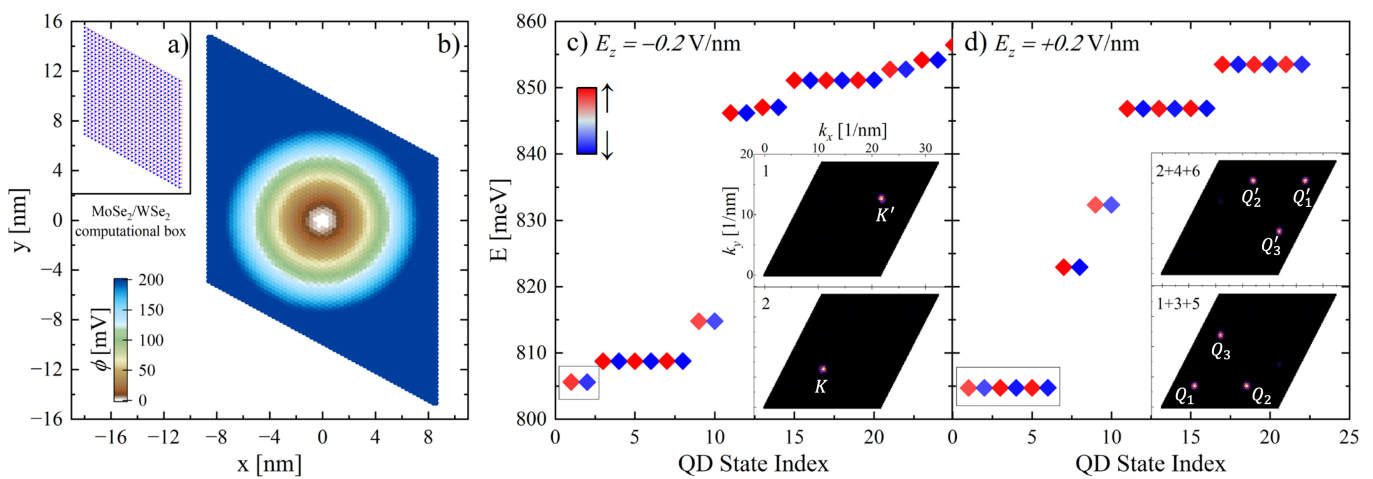


FIG. 7. (a) Scheme of the computational box in real space. (b) Electric potential ϕ profile of a Gaussian QD. (c) Spin-resolved QD energy spectrum for vertical electric field $E_z = -0.2$ V/nm and CB minimum located in the K valleys. (d) Analogous spectrum for $E_z = +0.2$ V/nm, for which CB minima are in Q points. Spin is indicated by color. The insets in panel (c) show density for the first $|\psi_1|^2$ and the second $|\psi_2|^2$ state, and the insets in panel (d) present two sums over states in the lowest shell in a specific spin subspace ($|\psi_1|^2 + |\psi_3|^2 + |\psi_5|^2$ and $|\psi_2|^2 + |\psi_4|^2 + |\psi_6|^2$, respectively).

notes the orbital, p corresponds to the band index, and $\phi_{\vec{k},l}^p(\vec{r})$ are the orbital Bloch functions build from the localized Slater orbitals. The QD states, expanded in the basis of low-energy band states $\varphi_{\vec{k}}^p$, are defined as:

$$\Phi^s(\vec{r}) = \sum_p \sum_{\vec{k}} B_{\vec{k}}^{s,p} \varphi_{\vec{k}}^p(\vec{r}), \quad (8)$$

where the summation is carried over the bands p and the wave vectors \vec{k} defined by the computational rhombus. The Schrödinger equation gives the integral equation for the amplitudes $B_{\vec{k}}^{s,p}$:

$$\epsilon_{\vec{k}}^p B_{\vec{k}}^{s,p} + \sum_{p',\vec{k}'} \langle \varphi_{\vec{k}}^p | V_{\text{QD}} | \varphi_{\vec{k}'}^{p'} \rangle B_{\vec{k}'}^{s,p'} = \epsilon^s B_{\vec{k}}^{s,p}, \quad (9)$$

with $\epsilon_{\vec{k}}^p$ denoting the single-particle energies of the heterostructure Hamiltonian described by Eq. (3). The coupling between the band states due to the confinement potential V_{QD} is determined by the matrix elements given as:

$$\langle \varphi_{\vec{k}}^p | V_{\text{QD}} | \varphi_{\vec{k}'}^{p'} \rangle = \sum_l \left(A_{\vec{k},l}^p \right)^* A_{\vec{k}',l}^{p'} e^{i(\vec{k}' - \vec{k}) \cdot \vec{\tau}_l} V_{\vec{k},\vec{k}',l}. \quad (10)$$

Here $\vec{\tau}_l$ corresponds to the position of orbitals within a UC, while $V_{\vec{k},\vec{k}',l}$ is the Fourier transform of the QD potential.

The eigenenergies and eigenstates of the QD system, denoted as ϵ^s and Φ^s , respectively, are determined by solving Eq. (9). The QD potential is modeled as a Gaussian potential characterized by a width of $\sigma_{\text{QD}} = 5$ nm and an amplitude of $U_{\text{QD}} = 300$ mV. In our calculations, we restrict p, p' to the two lowest CBs. Figure 7(c,d) illustrates the spin-resolved QD energy spectrum for two

directions of an applied vertical electric field E_z . When a negative electric field is applied, electrons localize in the K and K' valleys, resulting in a doubly degenerate shell of lowest-energy states, as shown in Fig. 7(c). The wavefunctions for these states are confined within the K/K' valleys, as illustrated in the insets of Fig. 7(c). The second shell originates from the secondary (higher) CB minimum at the 6 Q points. The third shell, also doubly degenerate, arises from the spin-split bands at the K points. The degeneracies of higher-energy shells can be understood in terms of the Fock-Darwin spectrum, including doubly degenerate $2p-2p$ states at the K points (four states in total) and $2p-2p$ states from the Q valleys (2×6 states in total), and further states following the same pattern.

Applying a positive electric field shifts electron localization from the K to the Q valleys, resulting in a 6-fold degenerate low-energy shell of QD states, as shown in Fig. 7(d). In this configuration, the wavefunctions for each spin subspace form a superposition across all three Q valleys, as illustrated in the insets of Fig. 7(d). The second and third shells are doubly degenerate, originating from spin-split bands around the K points. This behavior aligns with the reversal of valley character (Q vs. K) in successive shells, which governs their degeneracy.

VI. SUMMARY

In summary, we developed here a theory of a laterally gated quantum dot in an electrically tunable WSe₂/MoSe₂ heterostructure. We employed *ab initio* methods and derived a tight binding model to determine the tunability of valley contributions to the electronic structure of the WSe₂/MoSe₂ heterostructure with elec-

tric field. Our analysis revealed a type-II band alignment with energetically close CB minima at the K and Q points. We characterized the electronic properties, including the microscopic details of the layer, spin, and orbital contributions. Building on these results, we developed and parametrized a tight-binding model to describe the heterostructure, capturing the interplay between the two types of valleys in the CB. Furthermore, we explored the effect of a vertical electric field on the low-energy valley character of the CB minimum and VB maximum, validating our findings against the DFT calculations. Using the TB model, we studied a laterally gated quantum dot. We demonstrated that the QD energy spectrum can be effectively tuned by an applied vertical electric field, enabling control over the valley character of the low-energy states between K -valley 2-fold and Q -valley 6-fold degenerate configurations.

VII. ACKNOWLEDGMENTS

We thank M. Korkusiński, J. Fabian, D. Miravet and Y. Saleem for fruitful discussions. This research was supported by the National Science Centre, Poland, under Grant No. 2021/43/D/ST3/01989, and Digital Research Alliance Canada with computing resources, as well as by PLGrid (WCSS) high-performance computing infrastructure. P.H. acknowledges financial support from the Quantum Sensors Challenge Program QSP078 and Applied Quantum Computing AQC004 Challenge Programs at the National Research Council of Canada, NSERC Discovery Grant No. RGPIN- 2019-05714, and University of Ottawa Research Chair in Quantum Theory of Materials, Nanostructures, and Devices. P.E.F.J. acknowledges the financial support of the Deutsche Forschungsgemeinschaft (DFG, German Research Foundation) SFB 1277 (Project ID No. 314695032, Projects No. B07 and No. B11) and SPP 2244 (Project ID No. 443416183).

APPENDIX

Appendix A: DFT study details

The energies and wavefunctions have been calculated with the use of DFT methods, as implemented in Abinit [145]. Perdew-Burke-Ernzerhof (PBE) parametrization of the generalized gradient approximation (GGA) for both the exchange-correlation potentials [146] and the projector augmented wave (PAW) method [147] has been used. Both the atomistic spin-orbit interaction and the vdW interactions have been taken into account, where for vdW interactions the DFT-D3 exchange-correlation functional [148] has been applied. The PBE parametrization has been used with a plane-wave cutoff set to 160 Ha, the energy cutoff of 80 Ha, and the k -points grid $16 \times 16 \times 1$, respectively. Vacuum between the primitive cells along z -direction has been set to 40 Å. We have determined the

lattice constant to be $a = 3.323$ Å, while the chalcogen atoms distances in z direction are $d_{XX}^{\text{MoSe}_2} = 3.398$ Å and $d_{XX}^{\text{WSe}_2} = 3.360$ Å, and metal-chalcogen distances are $d_{MX}^{\text{MoSe}_2} = 2.542$ Å and $d_{MX}^{\text{WSe}_2} = 2.550$ Å, respectively. We note that throughout this paper the eigenenergies are shifted such that the Fermi energy is always $E_F = 0$. Electric field results were obtained as outlined in Ref. [134].

Subsequently, we study the general properties of the DFT Kohn-Sham wavefunctions $\varphi_k^{n,\text{DFT}}$, where n denotes bands and k denotes points from the reciprocal space. We define a density $\rho_k^n(z) = \iint_{UC} |\varphi_k^{n,\text{DFT}}(x, y, z)|^2 dx dy$ allowing us to determine the microscopic details of the leading spin and layer contributions, described in Section II.

In the next step, we calculate the orbital contributions to the energy bands of the MoSe₂/WSe₂ heterostructure using the Kohn-Sham wavefunctions projected onto Slater orbitals. The Slater-like localized orbitals are

$$\psi_l(\vec{r}) = \psi_{nLm}(\vec{r}) = R_{n,L}(r) Y_{Lm}(\theta, \phi), \quad (\text{A1})$$

where n , L and m denote the main, orbital angular momentum and magnetic quantum numbers. The radial function $R_{n,L}$ has been approximated as

$$R_{n,L}(r) = \frac{(2\zeta_{n,L})^{n+\frac{1}{2}}}{\sqrt{(2n)!}} r^{n-1} e^{-\zeta_{n,L}r}, \quad (\text{A2})$$

where the Slater parameters $\zeta_{n,L}$ being taken for the isolated atom model, specifically (in inverse Bohr radius units [a_0^{-1}]) $\zeta_{4p,Se} = 2.0718$, $\zeta_{4d,Mo} = 3.111$ and $\zeta_{5d,W} = 3.3484$ [149, 150]. Spherical harmonics $Y_{L,\mu}$ are given by the formula

$$Y_{L,m}(\theta, \phi) = \sqrt{\frac{2L+1}{4\pi} \frac{(L-m)!}{(L+m)!}} P_L^m(\cos\theta) e^{im\phi}. \quad (\text{A3})$$

In the above expression P_L^m are the associated Legendre polynomials with Condon-Shortley phase $(-1)^m$ included. For molybdenum and tungsten atoms we have $L = 2$ and $m \in \{-2, 0, +2\}$. For selenium atoms with $L = 1$ we have $m \in \{-1, 0, +1\}$. We note that for each layer top and bottom Se atoms have been treated as a dimer Se₂. We calculate the overlap of Kohn-Sham wavefunctions with TB-localized orbitals in spheres surrounding atoms, which radius is half of the distance to the nearest atom. All orbital compositions are normalized to 100% within valence shell orbitals space. All the main orbital contributions to the top VB and bottom CB are presented in Tab. I.

Appendix B: Details on the single layer tight-binding Hamiltonian

In Section IIID we have presented the heterostructure Hamiltonian given by Eq. (3), that contains the

TABLE I. Orbital contribution from DFT for the even subspace presented for the atomic orbitals with the main contribution to the top VB and bottom CB. Numbers are represented in % for a given high symmetry point. Sign '-' represents 0%/0% contribution.

		K, VB ↓/↑	K, CB ↓/↑	Q, CB ↓/↑	Γ, VB ↓/↑
Se ₂ ^(l_{top})	4p ₋₁	-	0%/20%	3%/1%	-
	4p ₀	-	-	4%/1%	6%/6%
	4p ₊₁	4%/0%	-	6%/2%	-
Mo	4d ₋₂	-	-	14%/5%	1%/0%
	4d ₀	-	0%/73%	8%/2%	11%/11%
	4d ₊₂	8%/0%	-	3%/1%	0%/1%
Se ₂ ^(l_{bottom})	4p ₋₁	27%/0%	-	6%/1%	-
	4p ₀	-	-	3%/1%	6%/6%
	4p ₊₁	-	-	2%/1%	-
W	5d ₋₂	53%/0%	-	2%/2%	1%/0%
	5d ₀	-	2%/0%	5%/1%	11%/11%
	5d ₊₂	-	0%/1%	11%/1%	0%/1%

blocks corresponding to the MoSe₂ and WSe₂ monolayers and the interlayer coupling between them, H_{inter} . Both monolayer TB models correspond to the minimal p^3d^5 *ab initio*-based TB described in our previous works [7–9, 31]. However, we have highlighted the need to modify one of those blocks due to the AB-stacking presented in Fig. 1(b) and considered throughout this study. This geometry corresponds to the 180° in-plane rotation of one layer with respect to the other. Hence, the TB Hamiltonian for one of the TMDC monolayers has to be modified accordingly, which results in the difference between $H_{\text{MoSe}_2}^{\text{rot}}$ and H_{WSe_2} defined in Eq. (3).

In the case of non-rotated layer (denoted here by the superscript (0)), the monolayer NNN Hamiltonian can be defined in a block form for both even and odd subspace as [7–9]:

$$H^{(0)} = \begin{bmatrix} H_{M-M}^{(0),\text{ev}} & H_{M-X_2}^{(0),\text{ev}} & 0 & 0 \\ H_{X_2-X_2}^{(0),\text{ev}} & 0 & 0 & 0 \\ 0 & 0 & H_{M-M}^{(0),\text{odd}} & H_{M-X_2}^{(0),\text{odd}} \\ 0 & 0 & H_{X_2-X_2}^{(0),\text{odd}} & 0 \end{bmatrix}. \quad (\text{B1})$$

Furthermore, the matrix describing metal-metal NNN interactions in the even subspace is given by:

$$H_{M-M}^{(0),\text{ev}} = \begin{bmatrix} E_{m_d=-2} & W_3g_2(\vec{k}) & W_4g_4(\vec{k}) \\ +W_{1g_0}(\vec{k}) & E_{m_d=0} & W_3g_2(\vec{k}) \\ & +W_{2g_0}(\vec{k}) & E_{m_d=2} \\ & & +W_{1g_0}(\vec{k}) \end{bmatrix}, \quad (\text{B2})$$

and in the odd subspace by:

$$H_{M-M}^{(0),\text{odd}} = \begin{bmatrix} E_{m_d=-1} & -W_9g_2(\vec{k}) \\ +W_{8g_0}(\vec{k}) & E_{m_d=+1} \\ & +W_{8g_0}(\vec{k}) \end{bmatrix}. \quad (\text{B3})$$

Next, the corresponding matrix describing X_2 - X_2 dimer interactions in the even subspace is defined as:

$$H_{X_2-X_2}^{(0),\text{ev}} = \begin{bmatrix} E_{m_p=-1} & 0 & -W_7g_2(\vec{k}) \\ +W_{5g_0}(\vec{k}) & E_{m_p=0} & 0 \\ & +W_{6g_0}(\vec{k}) & E_{m_p=1} \\ & & +W_{5g_0}(\vec{k}) \end{bmatrix}, \quad (\text{B4})$$

and in the odd subspace:

$$H_{X_2-X_2}^{(0),\text{odd}} = \begin{bmatrix} E_{m_p^{\text{odd}}=-1} & 0 & -W_7g_2(\vec{k}) \\ +W_{5g_0}(\vec{k}) & E_{m_p^{\text{odd}}=0} & 0 \\ & +W_{6g_0}(\vec{k}) & E_{m_p^{\text{odd}}=1} \\ & & +W_{5g_0}(\vec{k}) \end{bmatrix}, \quad (\text{B5})$$

Finally, the metal-dimer tunneling is described in the even subspace as:

$$H_{M-X_2}^{(0),\text{ev}} = \begin{bmatrix} V_1f_{-1}(\vec{k}) & -V_2f_0(\vec{k}) & V_3f_1(\vec{k}) \\ -V_4f_0(\vec{k}) & -V_5f_1(\vec{k}) & V_4f_{-1}(\vec{k}) \\ -V_3f_1(\vec{k}) & -V_2f_{-1}(\vec{k}) & -V_1f_0(\vec{k}) \end{bmatrix}, \quad (\text{B6})$$

and in the odd subspace:

$$H_{M-X_2}^{(0),\text{odd}} = \begin{bmatrix} -V_6f_{+1}(\vec{k}) & -V_8f_{-1}(\vec{k}) & V_7f_0(\vec{k}) \\ V_7f_{-1}(\vec{k}) & V_8f_0(\vec{k}) & -V_6f_{+1}(\vec{k}) \end{bmatrix}. \quad (\text{B7})$$

In the monolayer Hamiltonian given by Eq. (B1) the matrix elements of NN tunneling are expressed by k -independent parameters V_i :

$$\begin{aligned} V_1 &= \frac{1}{\sqrt{2}} \frac{d_{\parallel}}{d} \left[\frac{\sqrt{3}}{2} \left(\frac{d_{\perp}^2}{d^2} - 1 \right) V_{dp\sigma} - \left(\frac{d_{\perp}^2}{d^2} + 1 \right) V_{dp\pi} \right], \\ V_2 &= \frac{1}{2} \left(\frac{d_{\parallel}}{d} \right)^2 \frac{d_{\perp}}{d} \left[\sqrt{3} V_{dp\sigma} - 2V_{dp\pi} \right], \\ V_3 &= \frac{1}{\sqrt{2}} \left(\frac{d_{\parallel}}{d} \right)^3 \left[\frac{\sqrt{3}}{2} V_{dp\sigma} - V_{dp\pi} \right], \\ V_4 &= \frac{1}{2} \frac{d_{\parallel}}{d} \left[\left(3 \frac{d_{\perp}^2}{d^2} - 1 \right) V_{dp\sigma} - 2\sqrt{3} \frac{d_{\perp}^2}{d^2} V_{dp\pi} \right], \\ V_5 &= \frac{1}{\sqrt{2}} \frac{d_{\perp}}{d} \left[\left(3 \frac{d_{\perp}^2}{d^2} - 1 \right) V_{dp\sigma} - 2\sqrt{3} \left(\frac{d_{\perp}^2}{d^2} - 1 \right) V_{dp\pi} \right], \\ V_6 &= \frac{1}{\sqrt{2}} \frac{d_{\perp}}{d} \left[\frac{d_{\parallel}^2}{d^3} \left(\sqrt{3} V_{dp\sigma} - 2V_{dp\pi} \right) + 2V_{dp\pi} \right], \\ V_7 &= \frac{1}{\sqrt{2}} \frac{d_{\perp} d_{\parallel}^2}{d^3} \left(\sqrt{3} V_{dp\sigma} - 2V_{dp\pi} \right), \\ V_8 &= \frac{d_{\parallel}}{d} \left[\frac{d_{\perp}^2}{d^2} \left(\sqrt{3} V_{dp\sigma} - 2V_{dp\pi} \right) + V_{dp\pi} \right], \end{aligned} \quad (\text{B8})$$

and k -dependent functions f_i :

$$\begin{aligned}
f_{-1}(\vec{k}) &= e^{ik_x d_{\parallel}} + e^{-ik_x d_{\parallel}/2} e^{i\sqrt{3}k_y d_{\parallel}/2} e^{i2\pi/3} \\
&\quad + e^{-ik_x d_{\parallel}/2} e^{-i\sqrt{3}k_y d_{\parallel}/2} e^{-i2\pi/3}, \\
f_0(\vec{k}) &= e^{ik_x d_{\parallel}} + e^{-ik_x d_{\parallel}/2} e^{i\sqrt{3}k_y d_{\parallel}/2} e^{-i2\pi/3} \\
&\quad + e^{-ik_x d_{\parallel}/2} e^{-i\sqrt{3}k_y d_{\parallel}/2} e^{i2\pi/3}, \\
f_{+1}(\vec{k}) &= e^{ik_x d_{\parallel}} + e^{-ik_x d_{\parallel}/2} e^{i\sqrt{3}k_y/2} \\
&\quad + e^{-ik_x d_{\parallel}/2} e^{-i\sqrt{3}k_y/2}.
\end{aligned} \tag{B9}$$

The parameters of the NNN tunneling are given by k -independent terms W_i :

$$\begin{aligned}
W_1 &= \frac{1}{8} (3V_{dd\sigma} + 4V_{dd\pi} + V_{dd\delta}), \\
W_2 &= \frac{1}{4} (V_{dd\sigma} + 3V_{dd\delta}), \\
W_3 &= -\frac{\sqrt{3}}{4\sqrt{2}} (V_{dd\sigma} - V_{dd\delta}), \\
W_4 &= \frac{1}{8} (3V_{dd\sigma} - 4V_{dd\pi} + V_{dd\delta}), \\
W_5 &= \frac{1}{2} (V_{pp\sigma} + V_{pp\pi}), \\
W_6 &= V_{pp\pi}, \\
W_7 &= \frac{1}{2} (V_{pp\sigma} - V_{pp\pi}), \\
W_8 &= \frac{1}{2} (V_{dd\pi} + V_{dd\delta}), \\
W_9 &= \frac{1}{2} (V_{dd\pi} - V_{dd\delta}),
\end{aligned} \tag{B10}$$

and k -dependent functions g_i

$$\begin{aligned}
g_0(\vec{k}) &= 4 \cos(3k_x d_{\parallel}/2) \cos(\sqrt{3}k_y d_{\parallel}/2) + \\
&\quad 2 \cos(\sqrt{3}k_y d_{\parallel}), \\
g_2(\vec{k}) &= 2 \cos(3k_x d_{\parallel}/2 + \sqrt{3}k_y d_{\parallel}/2) e^{i\pi/3} + \\
&\quad 2 \cos(3k_x d_{\parallel}/2 - \sqrt{3}k_y d_{\parallel}/2) e^{-i\pi/3} + \\
&\quad - 2 \cos(\sqrt{3}k_y d_{\parallel}), \\
g_4(\vec{k}) &= 2 \cos(3k_x d_{\parallel}/2 + \sqrt{3}k_y d_{\parallel}/2) e^{i2\pi/3} + \\
&\quad 2 \cos(3k_x d_{\parallel}/2 - \sqrt{3}k_y d_{\parallel}/2) e^{-i2\pi/3} + \\
&\quad 2 \cos(\sqrt{3}k_y d_{\parallel}).
\end{aligned} \tag{B11}$$

Having fully defined the non-rotated monolayer TMDC NNN TB model, we now move to describing the differences that appear in the Hamiltonian due to the π in-plane rotation of one layer with respect to the other. We note that the rotation does not change neither the formulas defining the \vec{k} -dependent functions f and g , nor the definitions of amplitudes V and W . However, it results

in the change of the sign in \vec{k} coordinates for the NN couplings ($\vec{k} \rightarrow -\vec{k}$ for the metal-chalcogen dimer couplings) and does introduce a (-1) factor in front of the particular NN Hamiltonian matrix elements (the metal-chalcogen dimer couplings). Full Hamiltonian for rotated monolayer reads

$$H^{(\pi)} = \begin{bmatrix} H_{M-M}^{(0),\text{ev}} & H_{M-X_2}^{(\pi),\text{ev}} & 0 & 0 \\ & H_{X_2-X_2}^{(0),\text{ev}} & 0 & 0 \\ & & H_{M-M}^{(0),\text{odd}} & H_{M-X_2}^{(\pi),\text{odd}} \\ & & & H_{X_2-X_2}^{(0),\text{odd}} \end{bmatrix}. \tag{B12}$$

Below we redefine explicitly the M - X_2 matrix elements in the rotated TMDC monolayer Hamiltonian $H^{(\pi)}$ in the even subspace:

$$H_{M-X_2}^{(\pi),\text{ev}} = \begin{bmatrix} -V_1 f_{-1}(-\vec{k}) & -V_2 f_0(-\vec{k}) & -V_3 f_1(-\vec{k}) \\ V_4 f_0(-\vec{k}) & -V_5 f_1(-\vec{k}) & -V_4 f_{-1}(-\vec{k}) \\ V_3 f_1(-\vec{k}) & -V_2 f_{-1}(-\vec{k}) & V_1 f_0(-\vec{k}) \end{bmatrix}, \tag{B13}$$

and in the odd subspace:

$$H_{M-X_2}^{(\pi),\text{odd}} = \begin{bmatrix} -V_6 f_{+1}(-\vec{k}) & V_8 f_{-1}(-\vec{k}) & V_7 f_0(-\vec{k}) \\ V_7 f_{-1}(-\vec{k}) & -V_8 f_0(-\vec{k}) & -V_6 f_{+1}(-\vec{k}) \end{bmatrix}, \tag{B14}$$

respectively.

Next, we discuss the SOC Hamiltonian, given by Eq. 2. The non-zero matrix elements of H_{\uparrow}^{ev} block are diagonal and given by $\text{diag}(-\lambda_M, 0, \lambda_M, -1/2\lambda_{X_2}, 0, 1/2\lambda_{X_2})$. The corresponding odd block $H_{\uparrow}^{\text{odd}}$ is also diagonal $\text{diag}(-1/2\lambda_M, 1/2\lambda_M, -1/2\lambda_{X_2}, 0, 1/2\lambda_{X_2})$. Blocks with opposite spin have opposite signs. Even-odd subspace coupling elements are $H_{\uparrow\downarrow}^{\text{ev-odd}}$ and $H_{\uparrow\downarrow}^{\text{odd-ev}}$. First block has four non-zero elements given by:

- $\langle m_d = -2 \uparrow, \text{ev} | \hat{H}_{\text{SOC}} | m_d = -1 \downarrow, \text{odd} \rangle = \lambda_M,$
- $\langle m_d = 0 \uparrow, \text{ev} | \hat{H}_{\text{SOC}} | m_d = 1 \downarrow, \text{odd} \rangle = \sqrt{3/2}\lambda_M,$
- $\langle m_p = -1 \uparrow, \text{ev} | \hat{H}_{\text{SOC}} | m_p = 0 \downarrow, \text{odd} \rangle = \sqrt{2}/2\lambda_{X_2},$
- $\langle m_p = 0 \uparrow, \text{ev} | \hat{H}_{\text{SOC}} | m_p = 1 \downarrow, \text{odd} \rangle = \sqrt{2}/2\lambda_{X_2}.$

The non-zero elements of the second block $H_{\uparrow\downarrow}^{\text{odd-ev}}$ are:

- $\langle m_d = -1 \uparrow, \text{odd} | \hat{H}_{\text{SOC}} | m_d = 0 \downarrow, \text{ev} \rangle = \sqrt{3/2}\lambda_M,$
- $\langle m_d = 1 \uparrow, \text{odd} | \hat{H}_{\text{SOC}} | m_d = 2 \downarrow, \text{ev} \rangle = \lambda_M,$
- $\langle m_p = -1 \uparrow, \text{odd} | \hat{H}_{\text{SOC}} | m_p = 0 \downarrow, \text{ev} \rangle = \sqrt{2}/2\lambda_{X_2},$
- $\langle m_p = 0 \uparrow, \text{odd} | \hat{H}_{\text{SOC}} | m_p = 1 \downarrow, \text{ev} \rangle = \sqrt{2}/2\lambda_{X_2}.$

Appendix C: Full interlayer tight-binding Hamiltonian

In the following section we present the details of the TB model for interlayer interaction. We define the interlayer

Hamiltonian in both even and odd subspace, as well as include the mixing between them, hence the H_{inter} can be written in the form given by Eq. (4). However, we note the following symmetries between particular couplings:

$$\begin{aligned}
H_{pp}^{\text{ev-ev}} &= H_{pp}^{\text{ev-odd}} = -H_{pp}^{\text{odd-odd}} = -H_{pp}^{\text{odd-ev}} = H_{pp}, \\
H_{pd}^{\text{ev-ev}} &= -H_{pd}^{\text{odd-odd}} = H_{pd}^{(1)}, \\
H_{pd}^{\text{ev-odd}} &= -H_{pd}^{\text{odd-ev}} = H_{pd}^{(2)}, \\
H_{dp}^{\text{ev-ev}} &= H_{dp}^{\text{ev-odd}} = H_{dp}^{(1)}, \\
H_{dp}^{\text{odd-odd}} &= H_{dp}^{\text{odd-ev}} = H_{dp}^{(2)},
\end{aligned} \tag{C1}$$

thus allowing us to write rewrite Eq. (4) in the following form:

$$H_{\text{inter}} = \begin{bmatrix} H_{dd}^{(1)} & H_{dp}^{(1)} & H_{dd}^{(2)} & H_{dp}^{(1)} \\ H_{pd}^{(1)} & H_{pp} & H_{pd}^{(2)} & H_{pp} \\ H_{dd}^{(3)} & H_{dp}^{(2)} & H_{dd}^{(4)} & H_{dp}^{(2)} \\ -H_{pd}^{(1)} & -H_{pp} & -H_{pd}^{(2)} & -H_{pp} \end{bmatrix}. \tag{C2}$$

For the p - p couplings, corresponding blocks are defined as:

$$H_{pp} = \begin{bmatrix} T_1 f_{+1}(\vec{k}) & -T_2 f_{-1}(\vec{k}) & T_3 f_0(\vec{k}) \\ T_2 f_0(\vec{k}) & T_4 f_{+1}(\vec{k}) & -T_2 f_{-1}(\vec{k}) \\ T_3 f_{-1}(\vec{k}) & T_2 f_0(\vec{k}) & T_1 f_{+1}(\vec{k}) \end{bmatrix} \tag{C3}$$

For the p - d and d - p couplings we have:

$$\begin{aligned}
H_{pd}^{(1)} &= \begin{bmatrix} 0 & 0 & 0 \\ 0 & T_5 & 0 \\ 0 & 0 & 0 \end{bmatrix}, & H_{dp}^{(1)} &= \begin{bmatrix} 0 & 0 & 0 \\ 0 & T_7 & 0 \\ 0 & 0 & 0 \end{bmatrix}, \\
H_{pd}^{(2)} &= \begin{bmatrix} T_6 & 0 \\ 0 & 0 \\ 0 & T_6 \end{bmatrix}, & H_{dp}^{(2)} &= \begin{bmatrix} T_8 & 0 & 0 \\ 0 & 0 & T_8 \end{bmatrix}.
\end{aligned} \tag{C4}$$

Finally, for the d - d couplings, we obtain:

$$\begin{aligned}
H_{dd}^{(1)} &= \begin{bmatrix} T_9 f_{+1}(-\vec{k}) & T_{10} f_0(-\vec{k}) & T_{11} f_{-1}(-\vec{k}) \\ T_{10} f_{-1}(-\vec{k}) & T_{12} f_{+1}(-\vec{k}) & T_{10} f_0(-\vec{k}) \\ T_{11} f_0(-\vec{k}) & T_{10} f_{-1}(-\vec{k}) & T_9 f_{+1}(-\vec{k}) \end{bmatrix}, \\
H_{dd}^{(2)} &= \begin{bmatrix} T_{13} f_{-1}(-\vec{k}) & T_{14} f_{+1}(-\vec{k}) \\ T_{15} f_0(-\vec{k}) & -T_{15} f_{-1}(-\vec{k}) \\ -T_{14} f_{+1}(-\vec{k}) & -T_{13} f_0(-\vec{k}) \end{bmatrix}, \\
H_{dd}^{(3)} &= \begin{bmatrix} T_{13} f_0(-\vec{k}) & T_{15} f_{-1}(-\vec{k}) & -T_{14} f_{+1}(-\vec{k}) \\ T_{14} f_{+1}(-\vec{k}) & -T_{15} f_0(-\vec{k}) & -T_{13} f_{-1}(-\vec{k}) \end{bmatrix}, \\
H_{dd}^{(4)} &= \begin{bmatrix} T_{16} f_{+1}(-\vec{k}) & T_{17} f_0(-\vec{k}) \\ T_{17} f_{-1}(-\vec{k}) & T_{16} f_{+1}(-\vec{k}) \end{bmatrix}
\end{aligned} \tag{C5}$$

In the above equations f are \vec{k} -dependent functions defined in the previous section, while the amplitudes T are described by the heterostructure geometry and Slater-Koster parameters. These amplitudes parametrize the interlayer Mo-W (subscript dd), Se_2 - Se_2 (subscript pp),

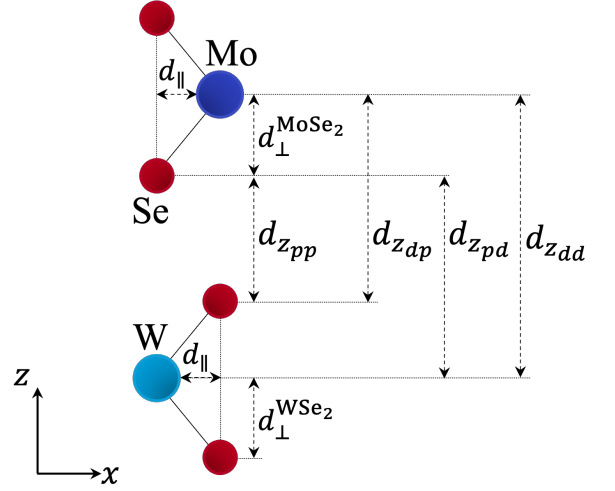


FIG. 8. Details of the geometric distances used in the TB model construction.

and metal-chalcogen (subscripts pd and dp) interactions, respectively. Additional distances on top of those presented in Fig. 1 are shown in Fig. 8. For clarity we introduce also the following distances: $d_{pp} = \sqrt{d_{zpp}^2 + d_{\parallel}^2}$, $d_{dd} = \sqrt{d_{zdd}^2 + d_{\parallel}^2}$, $d_{dp} = d_{zdp}$, $d_{pd} = d_{zpd}$, $d_{zdp} = d_{zdd} - d_{\perp}^{\text{WSe}_2}$, $d_{zpd} = d_{zdd} - d_{\perp}^{\text{MoSe}_2}$, $d_{zpp} = d_{zdd} - d_{\perp}^{\text{MoSe}_2} - d_{\perp}^{\text{WSe}_2}$. Numerical values we use are $d_{\perp} = 3.323/\sqrt{3}$ Å, $d_{\perp}^{\text{MoSe}_2} = 2.869$ Å, $d_{\perp}^{\text{WSe}_2} = 2.880$ Å, $d_{zdd} = 6.40$ Å. Below we present the formulas for each of the 17 amplitudes T . For the p - p couplings the amplitudes are defined as:

$$\begin{aligned}
T_1 &= \frac{1}{4} \left(\left[1 - \left(\frac{d_{zpp}}{d_{pp}} \right)^2 \right] V_{pp\sigma} + \left[1 + \left(\frac{d_{zpp}}{d_{pp}} \right)^2 \right] V_{pp\pi} \right), \\
T_2 &= \frac{1}{2\sqrt{2}} \frac{d_{\parallel} d_{zpp}}{d_{pp}^2} (V_{pp\sigma} - V_{pp\pi}), \\
T_3 &= -\frac{1}{4} \left(\frac{d_{\parallel}}{d_{pp}} \right)^2 (V_{pp\sigma} - V_{pp\pi}), \\
T_4 &= -\frac{1}{2} \left(\left(\frac{d_{zpp}}{d_{pp}} \right)^2 V_{pp\sigma} + \left(1 - \left(\frac{d_{zpp}}{d_{pp}} \right)^2 \right) V_{pp\pi} \right),
\end{aligned} \tag{C6}$$

Next, for the p - d and d - p couplings:

$$\begin{aligned}
T_5 &= \frac{1}{\sqrt{2}} V_{pd\sigma}, \\
T_6 &= -\frac{1}{\sqrt{2}} V_{pd\pi}, \\
T_7 &= \frac{1}{\sqrt{2}} V_{dp\sigma}, \\
T_8 &= \frac{1}{\sqrt{2}} V_{dp\pi}.
\end{aligned} \tag{C7}$$

Finally, in the case of d - d couplings:

$$\begin{aligned}
T_9 &= \frac{1}{8} \left[\left(3 - 6 \left(\frac{d_{zdd}}{d_{dd}} \right)^2 + 3 \left(\frac{d_{zdd}}{d_{dd}} \right)^4 \right) V_{dd\sigma} + \left(4 - 4 \left(\frac{d_{zdd}}{d_{dd}} \right)^4 \right) V_{dd\pi} + \left(1 + 6 \left(\frac{d_{zdd}}{d_{dd}} \right)^2 + \left(\frac{d}{d_{dd}} \right)^4 \right) V_{dd\delta} \right], \\
T_{10} &= \frac{1}{4} \sqrt{\frac{3}{2}} \left(\frac{d_{\parallel}}{d_{dd}} \right)^2 \left[\left(-1 + 3 \left(\frac{d_{zdd}}{d_{dd}} \right)^2 \right) V_{dd\sigma} - 4 \left(\frac{d_{zdd}}{d_{dd}} \right)^2 V_{dd\pi} + \left(1 + \left(\frac{d_{zdd}}{d_{dd}} \right)^2 \right) V_{dd\delta} \right], \\
T_{11} &= \frac{1}{8} \left(\frac{d_{\parallel}}{d_{dd}} \right)^4 (3V_{dd\sigma} - 4V_{dd\pi} + V_{dd\delta}), \\
T_{12} &= \frac{1}{4} \left[\left(1 - 6 \left(\frac{d_{zdd}}{d_{dd}} \right)^2 + 9 \left(\frac{d_{zdd}}{d_{dd}} \right)^4 \right) V_{dd\sigma} + 12 \left(\left(\frac{d_{zdd}}{d_{dd}} \right)^2 - \left(\frac{d_{zdd}}{d_{dd}} \right)^4 \right) V_{dd\pi} + \left(3 - 6 \left(\frac{d_{zdd}}{d_{dd}} \right)^2 + 3 \left(\frac{d_{zdd}}{d_{dd}} \right)^4 \right) V_{dd\delta} \right], \\
T_{13} &= \frac{1}{4} \frac{d_{\parallel}}{d_{dd}} \frac{d_{zdd}}{d_{dd}} \left[\left(3 - 3 \left(\frac{d_{zdd}}{d_{dd}} \right)^2 \right) V_{dd\sigma} + 4 \left(\frac{d_{zdd}}{d_{dd}} \right)^2 V_{dd\pi} - \left(3 + \left(\frac{d_{zdd}}{d_{dd}} \right)^2 \right) V_{dd\delta} \right], \\
T_{14} &= -\frac{1}{4} \left(\frac{d_{\parallel}}{d_{dd}} \right)^3 \frac{d_{zdd}}{d_{dd}} (3V_{dd\sigma} - 4V_{dd\pi} + V_{dd\delta}), \\
T_{15} &= \frac{1}{2} \sqrt{\frac{3}{2}} \frac{d_{\parallel}}{d_{dd}} \frac{d_{zdd}}{d_{dd}} \left[\left(-1 + 3 \left(\frac{d_{zdd}}{d_{dd}} \right)^2 \right) V_{dd\sigma} + \left(2 - 4 \left(\frac{d_{zdd}}{d_{dd}} \right)^2 \right) V_{dd\pi} + \left(-1 + \left(\frac{d_{zdd}}{d_{dd}} \right)^2 \right) V_{dd\delta} \right], \\
T_{16} &= \frac{1}{2} \left[3 \left(\left(\frac{d_{zdd}}{d_{dd}} \right)^2 - \left(\frac{d_{zdd}}{d_{dd}} \right)^4 \right) V_{dd\sigma} + \left(1 - 3 \left(\frac{d_{zdd}}{d_{dd}} \right)^2 + 4 \left(\frac{d_{zdd}}{d_{dd}} \right)^4 \right) V_{dd\pi} + \left(1 - \left(\frac{d_{zdd}}{d_{dd}} \right)^4 \right) V_{dd\delta} \right], \\
T_{17} &= -\frac{1}{2} \left(\frac{d_{\parallel}}{d_{dd}} \right)^2 \left[3 \left(\frac{d_{zdd}}{d_{dd}} \right)^2 V_{dd\sigma} + \left(1 - 4 \left(\frac{d_{zdd}}{d_{dd}} \right)^2 \right) V_{dd\pi} + \left(-1 + \left(\frac{d_{zdd}}{d_{dd}} \right)^2 \right) V_{dd\delta} \right], \tag{C8}
\end{aligned}$$

The parameters of the full TB model for the MoSe₂/WSe₂ heterostructure are summarized in the Tab. II. Furthermore, in Tab. III we present the orbital contributions to the energy bands for the even subspace, presented for the atomic orbitals with the main contribution to the top VB and bottom CB.

Appendix D: Basis transformation for electric field

In Section IV we have introduced the electric field Hamiltonian for an applied homogeneous perpendicular electric field E_z . Here we present the details of the Hamiltonian transformation to the dimer basis for a monolayer electric field Hamiltonian block.

Starting with the single-atomic basis (each Se atom taken separately), where the Hamiltonian for a single layer of TMDC crystals can be defined more intuitively in the basis: $\{d_{-2}, d_0, d_2, p_{-1}^t, p_0^t, p_1^t, d_{-1}, d_1, p_{-1}^b, p_0^b, p_1^b\}$, where p^t and p^b correspond to p -orbitals on top and bottom Se atoms. The electric field Hamiltonian can be written explicitly for a given spin as an 11×11 matrix containing diagonal terms only $H_E^{\text{atom}} = \text{diag}(V_M, V_M, V_M, V_{X^t}, V_{X^t}, V_{X^t}, V_M, V_M, V_{X^b}, V_{X^b}, V_{X^b})$. To reformulate this Hamiltonian to form given in main text for basis using dimer orbitals, we construct the

unitary transformation matrix between the both bases:

$$\hat{U}_E = \frac{1}{\sqrt{2}} \begin{pmatrix} \sqrt{2} & 0 & 0 & 0 & 0 & 0 & 0 & 0 & 0 & 0 & 0 \\ 0 & \sqrt{2} & 0 & 0 & 0 & 0 & 0 & 0 & 0 & 0 & 0 \\ 0 & 0 & \sqrt{2} & 0 & 0 & 0 & 0 & 0 & 0 & 0 & 0 \\ 0 & 0 & 0 & 1 & 0 & 0 & 0 & 0 & 1 & 0 & 0 \\ 0 & 0 & 0 & 0 & 1 & 0 & 0 & 0 & 0 & -1 & 0 \\ 0 & 0 & 0 & 0 & 0 & 1 & 0 & 0 & 0 & 0 & 1 \\ 0 & 0 & 0 & 0 & 0 & 0 & \sqrt{2} & 0 & 0 & 0 & 0 \\ 0 & 0 & 0 & 0 & 0 & 0 & 0 & \sqrt{2} & 0 & 0 & 0 \\ 0 & 0 & 0 & 1 & 0 & 0 & 0 & 0 & -1 & 0 & 0 \\ 0 & 0 & 0 & 0 & 1 & 0 & 0 & 0 & 0 & 1 & 0 \\ 0 & 0 & 0 & 0 & 0 & 1 & 0 & 0 & 0 & 0 & -1 \end{pmatrix}. \tag{D1}$$

By acting the transformation matrix on the H_E^{atom} Hamiltonian, $\hat{U}_E \hat{H}_E^{\text{atom}} \hat{U}_E^{-1}$, we obtain the electric field Hamiltonian given by Eq. (6).

Appendix E: Simplified tight-binding model

Having the TB model taking into account all interlayer orbital interactions, we present a simplified approach reproducing main MoSe₂/WSe₂ heterostructure features known from DFT. Guided by the majority orbital contributions to the VB and CB at high symmetry points, we simplify the interlayer interactions Hamiltonian block H_{inter} , defined in Eq. (4), by taking into account only

TABLE II. Slater-Koster parameters for the MoSe₂/WSe₂ heterostructure in the full/simplified TB model.

	MoSe ₂	WSe ₂	interlayer
E_d	-0.140/-0.240	-0.220/-0.210	-
E_{p_1}	-5.060/-5.258	-4.234/-4.419	-
E_{p_0}	-5.268/-5.620	-4.620/-4.890	-
$V_{dp\sigma}$	-2.980/-2.976	-3.251/-3.262	-0.044/ -
$V_{pd\sigma}$	-	-	-1.344/ -
$V_{dp\pi}$	1.073/1.175	1.060/1.020	0.411/ -
$V_{pd\pi}$	-	-	-1.780/ -
$V_{dd\sigma}$	-1.028/-0.923	-1.240/-1.223	0.196/-0.500
$V_{dd\pi}$	0.838/0.751	0.817/0.860	-0.480/2.000
$V_{dd\delta}$	0.229/0.225	0.255/0.238	0.091/-0.330
$V_{pp\sigma}$	1.490/1.397	1.258/1.079	1.393/-1.101
$V_{pp\pi}$	-0.550/-0.468	-0.350/-0.366	-0.012/-0.155
$E_{p_1}^{\text{odd}}$	-5.051/-5.398	-4.132/-4.559	-
$E_{p_0}^{\text{odd}}$	-5.236/-5.598	-4.554/-5.029	-
E_d^{odd}	-0.112/-0.380	-0.032/-0.350	-
λ_M	0.093/0.093	0.236/0.236	-
λ_{X_2}	0.175/0.100	-0.275/-0.195	-

the p_0 - p_0 , d_0 - d_0 , d_{-2} - d_{+2} and d_{+2} - d_{-2} couplings from the even orbital subspace. This reduces the H_{inter} to the following form:

$$H_{\text{inter}} = \begin{bmatrix} H_{dd}^{\text{ev-ev}} & 0 & 0 & 0 \\ 0 & H_{pp}^{\text{ev-ev}} & 0 & 0 \\ 0 & 0 & 0 & 0 \\ 0 & 0 & 0 & 0 \end{bmatrix}, \quad (\text{E1})$$

where the coupling blocks $H_{dd}^{\text{ev-ev}}$ and $H_{pp}^{\text{ev-ev}}$ are simplified to

$$H_{dd}^{\text{ev-ev}} = \begin{bmatrix} 0 & 0 & T_{11}f_{-1}(-\vec{k}) \\ 0 & T_{12}f_{+1}(-\vec{k}) & 0 \\ T_{11}f_0(-\vec{k}) & 0 & 0 \end{bmatrix}, \quad (\text{E2})$$

and

$$H_{pp}^{\text{ev-ev}} = \begin{bmatrix} 0 & 0 & 0 \\ 0 & T_4f_{+1}(\vec{k}) & 0 \\ 0 & 0 & 0 \end{bmatrix} \quad (\text{E3})$$

Functions f and amplitudes T have been defined in the previous section.

This gives the 5 interlayer Slater-Koster parameters (compared to 9 for the full TB model) and 26 intralayer parameters (13 for each layer), creating the subspace of 31 Slater-Koster parameters that have to be

TABLE III. Orbital contribution from full TB model for the even subspace presented for the atomic orbitals with the main contribution to the top VB and bottom CB. Numbers are presented in % for a given high symmetry point.

		K, VB	K, CB	Q, CB	Γ , VB
		\downarrow/\uparrow	\downarrow/\uparrow	\downarrow/\uparrow	\downarrow/\uparrow
Se ₂ ^{top}	$4p_{-1}$	-	0%/12%	2%/0%	-
	$4p_0$	-	-	7%/1%	3%/3%
	$4p_{+1}$	-	-	1%/0%	-
Mo	$4d_{-2}$	-	-	13%/1%	-
	$4d_0$	-	0%/83%	11%/1%	32%/32%
	$4d_{+2}$	-	-	3%/0%	-
Se ₂ ^{bottom}	$4p_{-1}$	-	-	4%/0%	-
	$4p_0$	-	-	9%/0%	-
	$4p_{+1}$	-	-	1%/0%	-
W	$5d_{-2}$	97%/0%	-	1%/0%	-
	$5d_0$	-	1%/0%	17%/1%	15%/15%
	$5d_{+2}$	-	0%/1%	24%/0%	-

parametrized. In the Tab. II we present full and simplified TB model parameters. We keep the parameters for both even and odd blocks of monolayer Hamiltonians, however good results can be obtained in even-only subspace.

Fig. 9(a,b) presents the electronic structure obtained by diagonalizing the Hamiltonian with the simplified interlayer interactions. The type-II band alignment has been captured, with the direct K - K energy gap of the order of 1 eV. The dispersion is characterised by the degenerate CB minima in K and Q points, as well as the degenerate VB maxima in K and Γ points, and stays in good agreement with the DFT results. The effective masses around K valley are also consistent with DFT. The effect of spin-valley locking in close vicinity of the K valley has been obtained. The intralayer spin splittings due to the SOC in both CB and VB in K point are established to be for MoSe₂ $\Delta_{\text{SOC}}^{\text{CB}} = 12$ meV and $\Delta_{\text{SOC}}^{\text{VB}} = 189$ meV, while for WSe₂ $\Delta_{\text{SOC}}^{\text{CB}} = 30$ meV and $\Delta_{\text{SOC}}^{\text{VB}} = 521$ meV. However, the effects of spin mixing due to the interactions between even and odd orbitals have not been captured for the low-energy bands. Fig. 9(b) shows that the electron in Q valley is delocalized between distinct layers, nevertheless the delocalization is not captured quantitatively. Subsequently, we have performed the analysis of orbital contributions. We note that they stay in quantitative agreement with the full TB model results. This is understood from the fact that the low-energy bands are mainly composed of the even orbitals.

In the next step, following the methodology described in Section IV we perform a study of the electronic structure evolution as a function of applied electric field E_z .

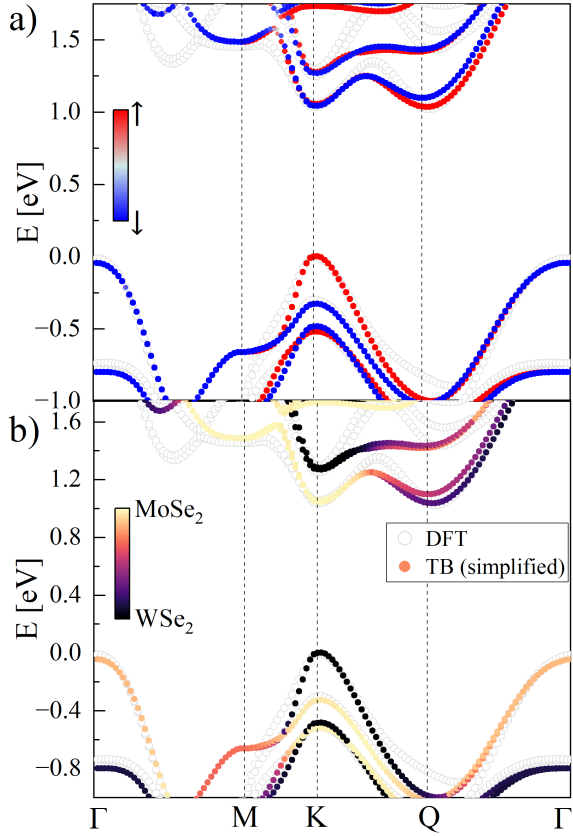


FIG. 9. Electronic structure of the MoSe₂/WSe₂ for the simplified TB model (full dots), presented in a comparison with DFT (open circles). The energy spectrum is presented on the Γ -M-K-Q- Γ path. The panels show (a) spin- and (b) layer-resolved electronic structures. Both spin and layer are decoded by color, where red/blue denotes spin up/down, while yellow/black denotes MoSe₂/WSe₂ layer, respectively.

The spin and layer contributions to the high symmetry points K , Q , and Γ for bands around the energy gap are presented on Fig. 10. We note that, unlike in the case of the full TB model, the applied electric field does not change the spin localization for both K and Q points. The CBs SOC splittings in K point are not affected by the applied E_z , while in the VB the splitting increase with the applied negative electric field, in agreement with the full TB model. As observed within DFT and full TB approximation, the spin-splitting between the two lowest CBs in Q point increases with the positive E_z and decreases with the negative E_z , respectively. Furthermore, the crossing of the CBs in the Q point as the negative applied E_z increases has been observed, changing the character of the K - Q energy gap. However, unlike in the case of full TB model, the effect of spin mixing around the crossing points have not been obtained.

In Fig. 10(b) we present the layer contribution. We note that the vertical electric field affects the coupling between layers, in agreement with the full TB model re-

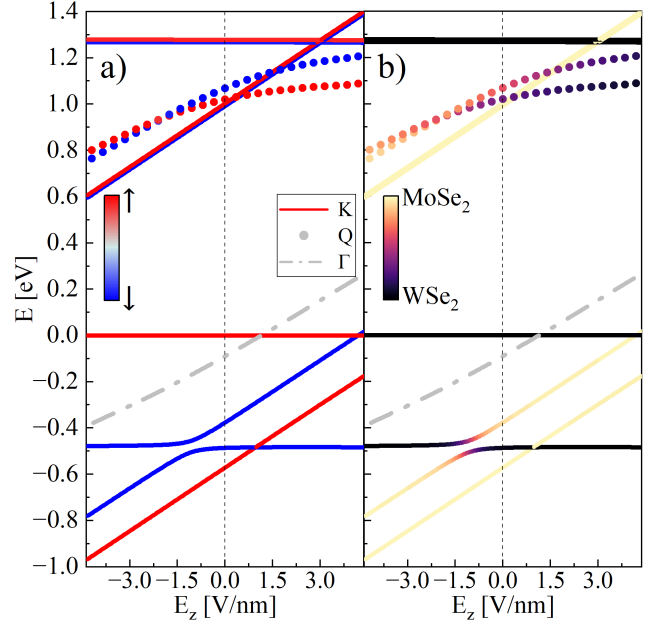


FIG. 10. The effect of a vertical electric field on the electronic structure in the simplified TB model. Energies of selected bands are presented as a function of the applied E_z for K , Q and Γ . The top of the VB in K is set to $E = 0$ eV. Different type of lines represent respectively K – continues line, Q – dashed line, Γ – dashed-dotted, as denoted on the scheme. colors correspond to (a) spin, and (b) layer composition, respectively. The color schemes are denoted on the plots. Due to the degeneracy of VB in the Γ point, the spin/layer-resolved notation was not introduced.

sults. However, we point out that the effect of switching the leading layer contribution obtained withing the simplified TB model has been captured not only in the Q point for the CBs, but also in the K point for the VBs, which stays in agreement with the DFT results. The intralayer energy gap for WSe₂ remains almost constant when applying the electric field, however the intralayer MoSe₂ energy gap changes due to the effects of layer mixing in the VB, which has not been observed in the full TB model. The direct interlayer energy gap decreases when applying E_z . Overall, DFT, full and simplified TB results agree on the character of the energy bands modulation with the applied electric field.

*

-
- [1] A. Splendiani, L. Sun, Y. Zhang, T. Li, J. Kim, C.-Y. Chim, G. Galli, and F. Wang, *Nano Letters* **10**, 1271 (2010).
- [2] K. F. Mak, C. Lee, J. Hone, J. Shan, and T. F. Heinz, *Phys. Rev. Lett.* **105**, 136805 (2010).
- [3] E. S. Kadantsev and P. Hawrylak, *Solid State Communications* **152**, 909 (2012).
- [4] G. Wang, A. Chernikov, M. M. Glazov, T. F. Heinz, X. Marie, T. Amand, and B. Urbaszek, *Rev. Mod. Phys.* **90**, 021001 (2018).
- [5] X. Liu and M. C. Hersam, *Nature Reviews Materials* **4**, 669 (2019).
- [6] D. Xiao, G.-B. Liu, W. Feng, X. Xu, and W. Yao, *Phys. Rev. Letters* **108**, 196802 (2012).
- [7] M. Bieniek, L. Szulakowska, and P. Hawrylak, *Phys. Rev. B* **101**, 125423 (2020).
- [8] M. Bieniek, M. Korkusiński, L. Szulakowska, P. Potasz, I. Ozfidan, and P. Hawrylak, *Phys. Rev. B* **97**, 085153 (2018).
- [9] M. Bieniek, K. Sadecka, L. Szulakowska, and P. Hawrylak, *Nanomaterials* **12** (2022).
- [10] J. Pawłowski, D. Żebrowski, and S. Bednarek, *Phys. Rev. B* **97**, 155412 (2018).
- [11] J. Pawłowski, *New Journal of Physics* **21**, 123029 (2019).
- [12] L. Szulakowska, M. Bieniek, and P. Hawrylak, *Solid-State Electronics* **155**, 105 (2019).
- [13] T. Scrace, Y. Tsai, B. Barman, L. Schweidenback, A. Petrou, G. Kioseoglou, I. Ozfidan, M. Korkusiński, and P. Hawrylak, *Nat. Nano.* **10**, 603 (2015).
- [14] A. Srivastava and A. m. c. Imamoğlu, *Phys. Rev. Lett.* **115**, 166802 (2015).
- [15] J. Zhou, W.-Y. Shan, W. Yao, and D. Xiao, *Phys. Rev. Lett.* **115**, 166803 (2015).
- [16] A. K. Geim and I. V. Grigorieva, *Nature* **499**, 419 (2013).
- [17] O. Ávalos Ovando, D. Mastrogiuseppe, and S. E. Ulloa, *Journal of Physics: Condensed Matter* **31**, 213001 (2019).
- [18] S. Gao, L. Yang, and C. D. Spataru, *Nano Letters* **17**, 7809 (2017).
- [19] E. Calman, M. Fogler, L. Butov, S. Hu, A. Mishchenko, and A. Geim, *Nature Commun.* **9**, 1 (2018).
- [20] L. A. Jauregui, A. Y. Joe, K. Pistunova, D. S. Wild, A. A. High, Y. Zhou, G. Scuri, K. De Greve, A. Sushko, C.-H. Yu, T. Taniguchi, K. Watanabe, D. J. Needleman, M. D. Lukin, H. Park, and P. Kim, *Science* **366**, 870 (2019).
- [21] W. Li, Z. Hadjri, L. M. Devenica, J. Zhang, S. Liu, J. Hone, K. Watanabe, T. Taniguchi, A. Rubio, and A. Srivastava, *Nature Materials* **22**, 1478 (2023).
- [22] L. H. Fowler-Gerace, Z. Zhou, E. A. Szwed, D. J. Choksy, and L. V. Butov, *Nature Photonics* **18**, 823 (2024).
- [23] H. Zeng, J. Dai, W. Yao, D. Xiao, and X. Cui, *Nature Nanotechnology* **7**, 490 (2012).
- [24] G.-B. Liu, W.-Y. Shan, Y. Yao, W. Yao, and D. Xiao, *Phys. Rev. B* **88**, 085433 (2013).
- [25] X.-X. Song, Z.-Z. Zhang, J. You, D. Liu, H.-O. Li, G. Cao, M. Xiao, and G.-P. Guo, *Scientific Reports* **5**, 16113 (2015).
- [26] X.-X. Song, D. Liu, V. Mosallanejad, J. You, T.-Y. Han, D.-T. Chen, H.-O. Li, G. Cao, M. Xiao, G.-C. Guo, *et al.*, *Nanoscale* **7**, 16867 (2015).
- [27] K. Lee, G. Kulkarni, and Z. Zhong, *Nanoscale* **8**, 7755 (2016).
- [28] K. Wang, K. De Greve, L. A. Jauregui, A. Sushko, A. High, Y. Zhou, G. Scuri, T. Taniguchi, K. Watanabe, M. D. Lukin, H. Park, and P. Kim, *Nature Nanotechnology* **13**, 128 (2018).
- [29] R. Pisoni, Z. Lei, P. Back, M. Eich, H. Overweg, Y. Lee, K. Watanabe, T. Taniguchi, T. Ihn, and K. Ensslin, *Applied Physics Letters* **112**, 123101 (2018).
- [30] S. Davari, J. Stacy, A. Mercado, J. Tull, R. Basnet, K. Pandey, K. Watanabe, T. Taniguchi, J. Hu, and H. Churchill, *Phys. Rev. Appl.* **13**, 054058 (2020).
- [31] A. Altıntaş, M. Bieniek, A. Dusko, M. Korkusiński, J. Pawłowski, and P. Hawrylak, *Phys. Rev. B* **104**, 195412 (2021).
- [32] J. Pawłowski, M. Bieniek, and T. Woźniak, *Phys. Rev. Appl.* **15**, 054025 (2021).
- [33] Y. Saleem, K. Sadecka, M. Korkusinski, D. Miravet, A. Dusko, and P. Hawrylak, *Nano Letters* **23**, 2998 (2023).
- [34] M. Korkusinski, Y. Saleem, A. Dusko, D. Miravet, and P. Hawrylak, *Nano Letters* **23**, 7546 (2023).
- [35] K. Sadecka, Y. Saleem, D. Miravet, M. Albert, M. Korkusinski, G. Bester, and P. Hawrylak, *Phys. Rev. B* **109**, 085434 (2024).
- [36] J. Pawłowski, J. E. Tiessen, R. Dax, and J. Shi, *Phys. Rev. B* **109**, 045411 (2024).
- [37] A. Y. Joe, K. Pistunova, K. Kaasbjerg, K. Wang, B. Kim, D. A. Rhodes, T. Taniguchi, K. Watanabe, J. Hone, T. Low, L. A. Jauregui, and P. Kim, *Phys. Rev. Lett.* **132**, 056303 (2024).
- [38] R. Krishnan, S. Biswas, Y.-L. Hsueh, H. Ma, R. Rahman, and B. Weber, *Nano Letters* **23**, 6171 (2023).
- [39] J. Boddison-Chouinard, A. Bogan, P. Barrios, J. Lapointe, K. Watanabe, T. Taniguchi, J. Pawłowski, D. Miravet, M. Bieniek, P. Hawrylak, A. Luican-Mayer, and L. Gaudreau, *npj 2D Materials and Applications* **7**, 50 (2023).
- [40] J. Pawłowski, D. Miravet, M. Bieniek, M. Korkusinski, J. Boddison-Chouinard, L. Gaudreau, A. Luican-Mayer, and P. Hawrylak, *Phys. Rev. B* **110**, 125147 (2024).
- [41] M. T. Björk, C. Thelander, A. E. Hansen, L. E. Jensen, M. W. Larsson, L. R. Wallenberg, and L. Samuelson, *Nano Letters* **4**, 1621 (2004).
- [42] A. Kormányos, V. Zólyomi, N. D. Drummond, and G. Burkard, *Phys. Rev. X* **4**, 011034 (2014).
- [43] L. Szulakowska, M. Cygorek, M. Bieniek, and P. Hawrylak, *Phys. Rev. B* **102**, 245410 (2020).
- [44] D. Miravet, A. Altıntaş, A. W. Rodrigues, M. Bieniek, M. Korkusinski, and P. Hawrylak, *Phys. Rev. B* **108**, 195407 (2023).
- [45] D. Miravet, L. Szulakowska, M. Bieniek, K. Sadecka,

- M. Korkusiński, and P. Hawrylak, *Phys. Rev. B* **110**, 235404 (2024).
- [46] P. Rivera, K. L. Seyler, H. Yu, J. R. Schaibley, J. Yan, D. G. Mandrus, W. Yao, and X. Xu, *Science* **351**, 688 (2016).
- [47] A. Ciarrocchi, D. Unuchek, A. Avsar, K. Watanabe, T. Taniguchi, and A. Kis, *Nature Photonics* **13**, 131 (2019).
- [48] K. L. Seyler, P. Rivera, H. Yu, N. P. Wilson, E. L. Ray, D. G. Mandrus, J. Yan, W. Yao, and X. Xu, *Nature* **567**, 66 (2019).
- [49] K. Tran, G. Moody, F. Wu, X. Lu, J. Choi, K. Kim, A. Rai, D. A. Sanchez, J. Quan, A. Singh, J. Embley, A. Zepeda, M. Campbell, T. Autry, T. Taniguchi, K. Watanabe, N. Lu, S. K. Banerjee, K. L. Silverman, S. Kim, E. Tutuc, L. Yang, A. H. MacDonald, and X. Li, *Nature* **567**, 71 (2019).
- [50] Z. Wang, D. A. Rhodes, K. Watanabe, T. Taniguchi, J. C. Hone, J. Shan, and K. F. Mak, *Nature* **574**, 76 (2019).
- [51] E. Y. Paik, L. Zhang, G. W. Burg, R. Gogna, E. Tutuc, and H. Deng, *Nature* **576**, 80 (2019).
- [52] D. Unuchek, A. Ciarrocchi, A. Avsar, Z. Sun, K. Watanabe, T. Taniguchi, and A. Kis, *Nature Nanotechnology* **14**, 1104 (2019).
- [53] F. Liu, W. Wu, Y. Bai, S. H. Chae, Q. Li, J. Wang, J. Hone, and X.-Y. Zhu, *Science* **367**, 903 (2020).
- [54] W. Li, X. Lu, S. Dubey, L. Devenica, and A. Srivastava, *Nature Materials* **19**, 624 (2020).
- [55] Y. Bai, L. Zhou, J. Wang, W. Wu, L. J. McGilly, D. Halbertal, C. F. B. Lo, F. Liu, J. Ardelean, P. Rivera, N. R. Finney, X.-C. Yang, D. N. Basov, W. Yao, X. Xu, J. Hone, A. N. Pasupathy, and X.-Y. Zhu, *Nature Materials* **19**, 1068 (2020).
- [56] W. Li, X. Lu, J. Wu, and A. Srivastava, *Nature Nanotechnology* **16**, 148 (2021).
- [57] J. Wang, Q. Shi, E.-M. Shih, L. Zhou, W. Wu, Y. Bai, D. Rhodes, K. Barmak, J. Hone, C. R. Dean, and X.-Y. Zhu, *Phys. Rev. Lett.* **126**, 106804 (2021).
- [58] E. Liu, E. Barré, J. van Baren, M. Wilson, T. Taniguchi, K. Watanabe, Y.-T. Cui, N. M. Gabor, T. F. Heinz, Y.-C. Chang, and C. H. Lui, *Nature* **594**, 46 (2021).
- [59] M. Brotons-Gisbert, H. Baek, A. Campbell, K. Watanabe, T. Taniguchi, and B. D. Gerardot, *Phys. Rev. X* **11**, 031033 (2021).
- [60] L. Ma, P. X. Nguyen, Z. Wang, Y. Zeng, K. Watanabe, T. Taniguchi, A. H. MacDonald, K. F. Mak, and J. Shan, *Nature* **598**, 585 (2021).
- [61] H. Baek, M. Brotons-Gisbert, A. Campbell, V. Vitale, J. Lischner, K. Watanabe, T. Taniguchi, and B. D. Gerardot, *Nature Nanotechnology* **16**, 1237 (2021).
- [62] X. Wang, J. Zhu, K. L. Seyler, P. Rivera, H. Zheng, Y. Wang, M. He, T. Taniguchi, K. Watanabe, J. Yan, D. G. Mandrus, D. R. Gamelin, W. Yao, and X. Xu, *Nature Nanotechnology* **16**, 1208 (2021).
- [63] N. P. Wilson, W. Yao, J. Shan, and X. Xu, *Nature* **599**, 383 (2021).
- [64] Z. Sun, A. Ciarrocchi, F. Tagarelli, J. F. Gonzalez Marin, K. Watanabe, T. Taniguchi, and A. Kis, *Nature Photonics* **16**, 79 (2022).
- [65] E. Barré, O. Karni, E. Liu, A. L. O’Beirne, X. Chen, H. B. Ribeiro, L. Yu, B. Kim, K. Watanabe, T. Taniguchi, K. Barmak, C. H. Lui, S. Refaely-Abramson, F. H. da Jornada, and T. F. Heinz, *Science* **376**, 406 (2022).
- [66] H. H. Yoon, H. A. Fernandez, F. Nigmatulin, W. Cai, Z. Yang, H. Cui, F. Ahmed, X. Cui, M. G. Uddin, E. D. Minot, H. Lipsanen, K. Kim, P. Hakonen, T. Hasan, and Z. Sun, *Science* **378**, 296 (2022).
- [67] M. Troue, J. Figueiredo, L. Sigl, C. Paspalides, M. Katzer, T. Taniguchi, K. Watanabe, M. Selig, A. Knorr, U. Wurstbauer, and A. W. Holleitner, *Phys. Rev. Lett.* **131**, 036902 (2023).
- [68] L. Du, M. R. Molas, Z. Huang, G. Zhang, F. Wang, and Z. Sun, *Science* **379**, eadg0014 (2023).
- [69] S. Zhao, Z. Li, X. Huang, A. Rupp, J. Göser, I. A. Vovk, S. Y. Kruchinin, K. Watanabe, T. Taniguchi, I. Bilgin, A. S. Baimuratov, and A. Högele, *Nature Nanotechnology* **18**, 572 (2023).
- [70] C. Hu, M. H. Naik, Y.-H. Chan, and S. G. Louie, *Phys. Rev. Lett.* **131**, 236904 (2023).
- [71] A. J. Campbell, V. Vitale, M. Brotons-Gisbert, H. Baek, A. Borel, T. V. Ivanova, T. Taniguchi, K. Watanabe, J. Lischner, and B. D. Gerardot, *Nature Physics* **20**, 589 (2024).
- [72] A. C. Johnson, J. D. Georganas, X. Shen, H. Yao, A. P. Saunders, H. J. Zeng, H. Kim, A. Sood, T. F. Heinz, A. M. Lindenberg, D. Luo, F. H. da Jornada, and F. Liu, *Science Advances* **10**, eadj8819 (2024).
- [73] C. Qian, M. Troue, J. Figueiredo, P. Soubelet, V. Villafañe, J. Beierlein, S. Klemmt, A. V. Stier, S. Höfling, A. W. Holleitner, and J. J. Finley, *Science Advances* **10**, eadk6359 (2024).
- [74] E. Wietek, M. Florian, J. Göser, T. Taniguchi, K. Watanabe, A. Högele, M. M. Glazov, A. Steinhoff, and A. Chernikov, *Phys. Rev. Lett.* **132**, 016202 (2024).
- [75] T.-S. Huang, P. Lunts, and M. Hafezi, *Phys. Rev. Lett.* **132**, 186202 (2024).
- [76] A. Y. Joe, A. M. Mier Valdivia, L. A. Jauregui, K. Pistunova, D. Ding, Y. Zhou, G. Scuri, K. De Greve, A. Sushko, B. Kim, T. Taniguchi, K. Watanabe, J. C. Hone, M. D. Lukin, H. Park, and P. Kim, *Nature Communications* **15**, 6743 (2024).
- [77] E. L. Peterson, T. I. Andersen, G. Scuri, A. Y. Joe, A. M. M. Valdivia, X. Liu, A. A. Zibrov, B. Kim, T. Taniguchi, K. Watanabe, J. Hone, V. Walther, H. Park, P. Kim, and M. D. Lukin, (2024), [arXiv:2407.11252](https://arxiv.org/abs/2407.11252).
- [78] P. Soubelet, A. Delhomme, A. V. Stier, and J. J. Finley, (2024), [arXiv:2407.15649](https://arxiv.org/abs/2407.15649).
- [79] H. E. Hannachi, M.-O. Goerbig, and S. Jaziri, (2024), [arXiv:2408.04136](https://arxiv.org/abs/2408.04136).
- [80] A. Steinhoff, E. Wietek, M. Florian, T. Schulz, T. Taniguchi, K. Watanabe, S. Zhao, A. Högele, F. Jahnke, and A. Chernikov, *Phys. Rev. X* **14**, 031025 (2024).
- [81] J. Wilson and A. Yoffe, *Advances in Physics* **18**, 193 (1969).
- [82] J. Choi, M. Florian, A. Steinhoff, D. Erben, K. Tran, D. S. Kim, L. Sun, J. Quan, R. Claassen, S. Majumder, J. A. Hollingsworth, T. Taniguchi, K. Watanabe, K. Ueno, A. Singh, G. Moody, F. Jahnke, and X. Li, *Phys. Rev. Lett.* **126**, 047401 (2021).
- [83] Z. Li, X. Lu, D. F. Cordovilla Leon, Z. Lyu, H. Xie, J. Hou, Y. Lu, X. Guo, A. Kaczmarek, T. Taniguchi, K. Watanabe, L. Zhao, L. Yang, and P. B. Deotare, *ACS nano* **15**, 1539 (2021).
- [84] F. Volmer, M. Ersfeld, P. E. Faria Junior, L. Waldecker,

- B. Parashar, L. Rathmann, S. Dubey, I. Cojocariu, V. Feyer, K. Watanabe, T. Taniguchi, C. M. Schneider, L. Plucinski, C. Stampfer, J. Fabian, and B. Beschoten, *npj 2D Materials and Applications* **7**, 58 (2023).
- [85] M. R. Rosenberger, H.-J. Chuang, M. Phillips, V. P. Oleshko, K. M. McCreary, S. V. Sivaram, C. S. Hellberg, and B. T. Jonker, *ACS Nano* **14**, 4550 (2020).
- [86] J.-H. Baek, H. G. Kim, S. Y. Lim, S. C. Hong, Y. Chang, H. Ryu, Y. Jung, H. Jang, J. Kim, Y. Zhang, K. Watanabe, T. Taniguchi, P. Y. Huang, H. Cheong, M. Kim, and G.-H. Lee, *Nature Materials* **22**, 1463 (2023).
- [87] A. Rupp, J. Göser, Z. Li, I. Bilgin, A. Baimuratov, and A. Högele, *2D Materials* **10**, 045028 (2023).
- [88] P. Rivera, J. R. Schaibley, A. M. Jones, J. S. Ross, S. Wu, G. Aivazian, P. Klement, K. Seyler, G. Clark, N. J. Ghimire, J. Yan, D. G. Mandrus, W. Yao, and X. Xu, *Nature Commun.* **6**, 1 (2015).
- [89] B. Miller, A. Steinhoff, B. Pano, J. Klein, F. Jahnke, A. Holleitner, and U. Würstbauer, *Nano Letters* **17**, 5229 (2017).
- [90] P. Nagler, M. V. Ballottin, A. A. Mitioglu, F. Mooshammer, N. Paradiso, C. Strunk, R. Huber, A. Chernikov, P. C. Christianen, C. Schüller, and T. Korn, *Nature Commun.* **8**, 1 (2017).
- [91] N. R. Wilson, P. V. Nguyen, K. Seyler, P. Rivera, A. J. Marsden, Z. P. L. Laker, G. C. Constantinescu, V. Kandyba, A. Barinov, N. D. M. Hine, X. Xu, and D. H. Cobden, *Science Advances* **3**, e1601832 (2017).
- [92] W.-T. Hsu, L.-S. Lu, P.-H. Wu, M.-H. Lee, P.-J. Chen, P.-Y. Wu, Y.-C. Chou, H.-T. Jeng, L.-J. Li, M.-W. Chu, and W.-H. Chang, *Nature Commun.* **9**, 1 (2018).
- [93] A. T. Hanbicki, H.-J. Chuang, M. R. Rosenberger, C. S. Hellberg, S. V. Sivaram, K. M. McCreary, I. I. Mazin, and B. T. Jonker, *Acs Nano* **12**, 4719 (2018).
- [94] J. Wang, J. Ardelean, Y. Bai, A. Steinhoff, M. Florian, F. Jahnke, X. Xu, M. Kira, J. Hone, and X.-Y. Zhu, *Science Advances* **5**, eaax0145 (2019).
- [95] T. Wang, S. Miao, Z. Li, Y. Meng, Z. Lu, Z. Lian, M. Blei, T. Taniguchi, K. Watanabe, S. Tongay, D. Smirnov, and S.-F. Shi, *Nano Letters* **20**, 694 (2019).
- [96] L. Zhang, R. Gogna, G. W. Burg, J. Horng, E. Paik, Y.-H. Chou, K. Kim, E. Tutuc, and H. Deng, *Phys. Rev. B* **100**, 041402 (2019).
- [97] J. Wang, J. Ardelean, Y. Bai, A. Steinhoff, M. Florian, F. Jahnke, X. Xu, M. Kira, J. Hone, and X.-Y. Zhu, *Science Advances* **5**, eaax0145 (2019).
- [98] E. Calman, L. Fowler-Gerace, D. Choksy, L. Butov, D. Nikonov, I. Young, S. Hu, A. Mishchenko, and A. Geim, *Nano Letters* **20**, 1869 (2020).
- [99] L. Sigl, F. Sigger, F. Kronowetter, J. Kiemle, J. Klein, K. Watanabe, T. Taniguchi, J. J. Finley, U. Würstbauer, and A. W. Holleitner, *Phys. Rev. Research* **2**, 042044 (2020).
- [100] A. Y. Joe, L. A. Jauregui, K. Pistunova, A. M. Mier Valdivia, Z. Lu, D. S. Wild, G. Scuri, K. De Greve, R. J. Gelly, Y. Zhou, J. Sung, A. Sushko, T. Taniguchi, K. Watanabe, D. Smirnov, M. D. Lukin, H. Park, and P. Kim, *Phys. Rev. B* **103**, L161411 (2021).
- [101] C. Li, A. V. Scherbakov, P. Soubelet, A. K. Samusev, C. Ruppert, N. Balakrishnan, V. E. Gusev, A. V. Stier, J. J. Finley, M. Bayer, and A. V. Akimov, *Nano Letters* **23**, 8186 (2023).
- [102] L. Yu, K. Pistunova, J. Hu, K. Watanabe, T. Taniguchi, and T. F. Heinz, *Nature Materials* **22**, 1485 (2023).
- [103] F. Mahdikhanyarvejahany, D. N. Shanks, M. Klein, Q. Wang, M. R. Koehler, D. G. Mandrus, T. Taniguchi, K. Watanabe, O. L. A. Monti, B. J. LeRoy, and J. R. Schaibley, *Nature Commun.* **13**, 5354 (2022).
- [104] H. Yu, Y. Wang, Q. Tong, X. Xu, and W. Yao, *Phys. Rev. Lett.* **115**, 187002 (2015).
- [105] J. R. Schaibley, H. Yu, G. Clark, P. Rivera, J. S. Ross, K. L. Seyler, W. Yao, and X. Xu, *Nature Reviews Materials* **1**, 16055 (2016).
- [106] H. Yu, G.-B. Liu, J. Tang, X. Xu, and W. Yao, *Science Advances* **3**, e1701696 (2017).
- [107] J. Cao, G. Gandus, T. Agarwal, M. Luisier, and Y. Lee, *Phys. Rev. Res.* **4**, 043073 (2022).
- [108] P. Merkl, F. Mooshammer, P. Steinleitner, A. Girnghuber, K.-Q. Lin, P. Nagler, J. Holler, C. Schüller, J. M. Lupton, T. Korn, S. Ovesen, S. Brem, E. Malic, and R. Huber, *Nature Materials* **18**, 691 (2019).
- [109] J. Kiemle, F. Sigger, M. Lorke, B. Miller, K. Watanabe, T. Taniguchi, A. Holleitner, and U. Würstbauer, *Phys. Rev. B* **101**, 121404 (2020).
- [110] T. L. Purz, E. W. Martin, P. Rivera, W. G. Holtzmann, X. Xu, and S. T. Cundiff, *Phys. Rev. B* **104**, L241302 (2021).
- [111] S. Miao, T. Wang, X. Huang, D. Chen, Z. Lian, C. Wang, M. Blei, T. Taniguchi, K. Watanabe, S. Tongay, Z. Wang, D. Xiao, Y.-T. Cui, and S.-F. Shi, *Nature Communications* **12**, 3608 (2021).
- [112] A. R.-P. Montblanch, M. Barbone, I. Aharonovich, M. Atatüre, and A. C. Ferrari, *Nature Nanotechnology* **18**, 555 (2023).
- [113] F. Wu, T. Lovorn, and A. H. MacDonald, *Phys. Rev. B* **97**, 035306 (2018).
- [114] R. Gillen and J. Maultzsch, *Phys. Rev. B* **97**, 165306 (2018).
- [115] E. Torun, H. P. Miranda, A. Molina-Sánchez, and L. Wirtz, *Phys. Rev. B* **97**, 245427 (2018).
- [116] M. Van der Donck and F. Peeters, *Phys. Rev. B* **98**, 115104 (2018).
- [117] T. Woźniak, P. E. Faria Junior, G. Seifert, A. Chaves, and J. Kunstmann, *Phys. Rev. B* **101**, 235408 (2020).
- [118] L. L. Li, R. Gillen, M. Palummo, M. V. Milošević, and F. M. Peeters, *Applied Physics Letters* **123**, 033102 (2023).
- [119] L. G. M. Tenório, T. A. S. Pereira, K. Mohseni, T. Frederico, M. R. Hadizadeh, D. R. da Costa, and A. J. Chaves, *Phys. Rev. B* **108**, 035421 (2023).
- [120] F. Wu, T. Lovorn, and A. H. MacDonald, *Phys. Rev. Lett.* **118**, 147401 (2017).
- [121] F. Wu, T. Lovorn, E. Tutuc, and A. H. MacDonald, *Phys. Rev. Lett.* **121**, 026402 (2018).
- [122] D. A. Ruiz-Tijerina and V. I. Fal'ko, *Phys. Rev. B* **99**, 125424 (2019).
- [123] V. Vitale, K. Atalar, A. A. Mostofi, and J. Lischner, *2D Materials* **8**, 045010 (2021).
- [124] E. Cappelluti, R. Roldán, J. A. Silva-Guillén, P. Ordejón, and F. Guinea, *Phys. Rev. B* **88**, 075409 (2013).
- [125] F. Zahid, L. Liu, Y. Zhu, J. Wang, and H. Guo, *AIP Advances* **3**, 052111 (2013).
- [126] R. Roldán, J. A. Silva-Guillén, M. P. López-Sancho, F. Guinea, E. Cappelluti, and P. Ordejón, *Annalen der Physik* **526**, 347 (2014).
- [127] S. Fang, R. Kuate Defo, S. N. Shirodkar, S. Lieu, G. A. Tritsarlis, and E. Kaxiras, *Phys. Rev. B* **92**, 205108 (2015).

- [128] K. V. Shanavas and S. Satpathy, *Phys. Rev. B* **91**, 235145 (2015).
- [129] S. Venkateswarlu, A. Honecker, and G. Trambly de Laisardière, *Phys. Rev. B* **102**, 081103 (2020).
- [130] Y. Zhang, Z. Zhan, F. Guinea, J. A. Silva-Guillén, and S. Yuan, *Phys. Rev. B* **102**, 235418 (2020).
- [131] J. He, K. Hummer, and C. Franchini, *Phys. Rev. B* **89**, 075409 (2014).
- [132] J. He, K. Hummer, and C. Franchini, *Phys. Rev. B* **89**, 075409 (2014).
- [133] K. Sadecka, *Acta Physica Polonica, A* **141** (2022).
- [134] P. E. Faria Junior and J. Fabian, *Nanomaterials* **13** (2023).
- [135] J. C. Slater and G. F. Koster, *Phys. Rev.* **94**, 1498 (1954).
- [136] K. V. Price, R. M. Storn, and J. A. Lampinen, *Differential evolution: A practical approach to global optimization* (Springer, 2005) pp. 37–134.
- [137] A. Laturia, M. L. Van de Put, and W. G. Vandenberghe, *npj 2D Materials and Applications* **2**, 6 (2018).
- [138] A. Varlet, D. Bischoff, P. Simonet, K. Watanabe, T. Taniguchi, T. Ihn, K. Ensslin, M. Mucha-Kruczyński, and V. I. Fal’ko, *Phys. Rev. Lett.* **113**, 116602 (2014).
- [139] A. Knothe and V. Fal’ko, *Phys. Rev. B* **101**, 235423 (2020).
- [140] M. Albert, D. Miravet, Y. Saleem, K. Sadecka, M. Korzukinski, G. Bester, and P. Hawrylak, *Phys. Rev. B* **110**, 155421 (2024).
- [141] H. Overweg, A. Knothe, T. Fabian, L. Linhart, P. Rickhaus, L. Wernli, K. Watanabe, T. Taniguchi, D. Sánchez, J. Burgdörfer, F. Libisch, V. I. Fal’ko, K. Ensslin, and T. Ihn, *Phys. Rev. Lett.* **121**, 257702 (2018).
- [142] R. Garreis, A. Knothe, C. Tong, M. Eich, C. Gold, K. Watanabe, T. Taniguchi, V. Fal’ko, T. Ihn, K. Ensslin, and A. Kurzmam, *Phys. Rev. Lett.* **126**, 147703 (2021).
- [143] A. M. Seiler, N. Jacobsen, M. Statz, N. Fernandez, F. Falorsi, K. Watanabe, T. Taniguchi, Z. Dong, L. S. Levitov, and R. T. Weitz, *Nature Communications* **15**, 3133 (2024).
- [144] M. Bieniek, L. Szulakowska, and P. Hawrylak, *Phys. Rev. B* **101**, 035401 (2020).
- [145] X. Gonze, J.-M. Beuken, R. Caracas, F. Detraux, M. Fuchs, G.-M. Rignanese, L. Sindic, M. Verstraete, G. Zerah, F. Jollet, M. Torrent, A. Roy, M. Mikami, P. Ghosez, J.-Y. Raty, and D. Allan, *Computational Materials Science* **25**, 478 (2002).
- [146] J. P. Perdew, K. Burke, and M. Ernzerhof, *Phys. Rev. Letter* **77**, 3865 (1996).
- [147] P. E. Blöchl, *Phys. Rev. B* **50**, 17953 (1994).
- [148] S. Grimme, J. Antony, S. Ehrlich, and H. Krieg, *The Journal of Chemical Physics* **132**, 154104 (2010).
- [149] E. Clementi and D. L. Raimondi, *The Journal of Chemical Physics* **38**, 2686 (1963).
- [150] E. Clementi, D. L. Raimondi, and W. P. Reinhardt, *The Journal of Chemical Physics* **47**, 1300 (1967).